Mechanics of Materials 176 (2023) 104510

Contents lists available at ScienceDirect

Mechanics of Materials

journal homepage: www.elsevier.com/locate/mecmat

Research paper

Effects of plastic strain and reloading stress on the magneto-mechanical behavior of electrical steels: Experiments and modeling

Mathieu Domenjoud, Laurent Daniel *

Université Paris-Saclay, CentraleSupélec, CNRS, Laboratoire de Génie Électrique et Électronique de Paris, 91192, Gif-sur-Yvette, France
Sorbonne Université, CNRS, Laboratoire de Génie Électrique et Électronique de Paris, 75252, Paris, France

ARTICLE INFO

Keywords:
Ferromagnetic materials
Anhysteretic measurement
Magneto-elasticity
Magneto-plasticity
Hardening
Internal stresses
Micro-mechanical modeling

ABSTRACT

The properties of electro-mechanical systems are intimately linked to the mechanical state of the materials used for their design. Notably, the processing stages can lead to significant mechanical stresses, with a strong impact on the final magnetic behavior, through plasticity and residual stress effects. This work presents a thorough magneto-mechanical characterization, both hysteretic and anhysteretic, of an electrical steel (DC04) at different levels of plastic deformation and applied tension stress. The mechanical characterization of the material leads to the identification of two hardening stages: a first stage attributed to the development of long-range internal back stress, and a second stage dominated by intragranular stresses connected to the formation of dislocation structures. The magnetic characterization shows that, under no applied stress, plastic strain involves a significant degradation of the magnetic behavior. Mechanical reloading allows recovering part of the magnetic properties of the virgin material. A simplified multiscale modeling tool is proposed for the magneto-mechanical behavior, including the effects of internal stress and dislocation density. The model is notably used to predict the effect of a reloading stress on the magnetic behavior of a plasticized material, with a very satisfactory agreement. For the first time, a three-dimensional modeling approach is proposed for the magneto-mechanical behavior of materials including levels of plasticity up to necking. The very low computation cost of the modeling approach makes it suitable for the numerical study of magnetic devices under various mechanical states. In addition, this formulation opens a route for estimating the mechanical state of a plastically deformed material through the analysis of its magnetic behavior.

1. Introduction[1]

Magnetic materials are widely used for the design of electrical machines, actuators, or transducers. The performance of these systems is highly dependent on the thermo-mechanical loadings experienced by the materials in operation or during the manufacturing process (e.g. cutting, welding, sticking, or punching) (Jiles, 1991; Ossart et al., 2000; Schoppa et al., 2003; Araujo et al., 2010; Shi et al., 2018; M'zali et al., 2021). Understanding and modeling the three-dimensional magneto-elasto-plastic effects are still open issues pulling electrical machine designers and manufacturers to make use of empirical building factors to account for them.

The impact of stress on magnetic properties has been the object of many research studies. Bozorth and Williams (1945) and Bozorth (1951) reported the changes in magnetization when elastic stress is applied to Nickel or Permalloy. Uniaxial tension can increase or decrease the initial permeability of the material depending on the sign of magnetostriction constants. Tension and compression have non-symmetrical effects. Plastic deformation causes the deterioration of the magnetic properties of electrical steels, especially at low strains (typically 0 to 5%) and low and medium magnetic field amplitudes (typically 0 to 5 kA m^{-1}) (Hug et al., 1996, 1997; Landgraf et al., 2020).

The impact of plasticity on the magnetic behavior is commonly explained as the consequence of plasticity on pinning/unpinning mechanisms (Makar and Tanner, 1998, 2000; Sablik, 2001; Emura et al., 2003; Sablik et al., 2004; Wang et al., 2011; Li et al., 2012; M'zali et al., 2020; Shi et al., 2020). Dislocations act as pinning centers for the magnetic domain walls. As the dislocation density increases, the barriers to wall motion are multiplied, and the energy required to reach a given level of magnetization is higher.

The development of internal stress induced by plastic strain can also explain the effect of plasticity on the degradation of magnetic properties. Cullity (1972) clarified the distribution of micro-stress induced by plastic deformation using X-ray measurements on a plastically

* Corresponding author.
E-mail address: laurent.daniel@centralesupelec.fr (L. Daniel).

[1] most notations used in the paper are summarised in Table 1.

https://doi.org/10.1016/j.mechmat.2022.104510
Received 30 April 2022; Received in revised form 25 October 2022; Accepted 25 October 2022
Available online 6 November 2022

Table 1
Main symbols used in the paper.

Symbol	Unit	Definition
$\mathbf{H}$	A m^{-1}	Macroscopic magnetic field vector (H its amplitude, $\mathbf{h}$ its direction : $\mathbf{H} = H\,\mathbf{h}$)
H_{anh}	A m^{-1}	Anhysteretic magnetic field amplitude
H_c	A m^{-1}	Coercive field (H_c^0 its value at the virgin state under no applied stress)
H_{max}	A m^{-1}	Maximal magnetic field amplitude
$\mathbf{B}$	T	Magnetic induction vector (B its amplitude)
B_{anh}	T	Anhysteretic magnetic induction amplitude
$B_{H_{max}}$	T	Magnetic induction at H_{max}
B_r	T	Remnant magnetic induction
$\mathbf{M}$	A m^{-1}	Macroscopic magnetization vector
$\mathbf{M}_\alpha$	A m^{-1}	Local magnetization vector (domain scale)
$\boldsymbol{\varepsilon}^\mu$	–	Macroscopic magnetostriction strain tensor
$\boldsymbol{\varepsilon}_\alpha^\mu$	–	Local magnetostriction strain tensor (domain scale)
$\varepsilon_{/\!/}$	–	True longitudinal strain (total strain)
$\varepsilon_{/\!/}^{\text{eng}}$	–	Engineering longitudinal strain (total strain)
ε_p	–	True longitudinal plastic strain (ε_p^n its value at necking)
$\boldsymbol{\sigma}$	N m^{-2}	Stress tensor (true stress)
$\boldsymbol{\sigma}_{app}$	N m^{-2}	Applied stress tensor (true stress)
σ_u	N m^{-2}	Amplitude of $\boldsymbol{\sigma}_{app}$ in the case of a uniaxial stress
$\sigma_u^{\max}$	N m^{-2}	For a given plastic strain level, maximum amplitude of σ_u before unloading
σ_{eq}	N m^{-2}	Equivalent deviatoric stress
W_α	J m^{-3}	Local free energy (domain scale)
W_α^{an}	J m^{-3}	Local anisotropy energy (domain scale)
W_α^{mag}	J m^{-3}	Local magnetostatic energy (domain scale)
W_α^{el}	J m^{-3}	Local magneto-elastic energy (domain scale)
$W_\alpha^{\text{el(1)}}$	J m^{-3}	First order local magneto-elastic energy (domain scale)
$W_\alpha^{\text{el(2)}}$	J m^{-3}	Second order local magneto-elastic energy (domain scale)
$\boldsymbol{\alpha}$		Unit vector defining the direction of the magnetization (domain scale)
f_α	–	Volume fraction of domains with orientation $\boldsymbol{\alpha}$
M_{sat}	A m^{-1}	Saturation magnetization
λ_{sat}	–	Saturation magnetostriction
λ'_{sat}	m^2 N^{-1}	Second-order magnetostrictive constant
σ_u^r	N m^{-2}	Reversal stress (value of uniaxial stress σ_u at which permeability starts decreasing)
μ_{anh}	–	Relative anhysteretic magnetic permeability (scalar)
χ_i	–	Initial anhysteretic magnetic susceptibility (scalar) (χ_i^0 its value at the virgin state under no applied stress)
A_s, A_s^0		Parameters of the simplified multiscale model
Y, R_e	N m^{-2}	Young modulus, and yield stress
HS_1, HS_2	–	First and second hardening stage
σ_{HS_1}, σ_{HS_2}	N m^{-2}	Hardening stress in HS_1 and HS_2
K_1, K_2	N m^{-2}	Resistance coefficient of Ludwik law in HS_1 and HS_2
m_1, m_2	–	Hardening power coefficient of Ludwik law in HS_1 and HS_2
σ_{int}	N m^{-2}	Internal back stress
N_d	m^{-2}	Dislocation density (N_d^0 its value at the virgin state)
η_1, η_2	–	
η_d, η_H	m^2 N^{-1}	
μ_0	H m^{-1}	Vacuum magnetic permeability
$\mathbf{I}$	–	Second-order identity tensor

elongated polycrystalline Iron (after removal of the mechanical loading): 90% of the sample volume was found to be subjected to residual compressive stress balanced by small regions under high tensile stress. Besides, it is well known that compressive stress leads to a drop in anhysteretic and hysteretic magnetic properties of ferromagnetic materials with positive magnetostriction (Jiles et al., 1984; Sablik et al., 1987; Sablik and Jiles, 1988; Domenjoud et al., 2019). Various works showed that magnetic behavior (Abuku, 1977), magnetostrictive behavior (Cullity, 1972) and Barkhausen signal (Gatelier-Rothea et al., 1998; Kleber and Vincent, 2004) of plastically deformed steels exhibit similarities with those of specimens under stress: materials plasticized under tension (respectively compression) stress behave similarly to elastically compressed (respectively stretched) samples.

Jiles (1988) investigated the effect of compressive plastic deformation on the magnetic properties of AISI 4130 steels with various microstructures. The initial magnetic permeability was found to decrease with plastic deformation, while the coercive field and hysteresis loss increased. It was concluded that compressive plastic deformation results in tensile residual stress throughout a large volume fraction of the material. Other works (Qureshi and Chaudhary, 1970; Lubitz, 1974) focused on the dislocation density N_d as the driving parameter for the evolution of coercive field H_c and initial susceptibility χ_i following plastic deformation in ferromagnetic materials. The results showed that H_c and $1/\chi_i$ vary approximately as $\sqrt{N_d}$, suggesting that the rearrangement of dislocations determines the effect on magnetic properties. Thompson and Tanner (1994) reported measurements of magnetic properties and Barkhausen noise emissions of pearlitic steels as a function of tensile plastic deformation. The changes in the magnetic properties were found to result from a combination of the magnetostrictive effects of residual compressive stress and the pinning effects of dislocation tangles. Hug et al. (1996, 2002) characterized the influence of the plastic anisotropy and internal stresses on the magnetic properties of non-oriented Iron–Silicon steels. The degradation of the magnetic properties with plastic strain was considered the result of two effects: a first one representative of the metallurgical defects created by strengthening and a second one due to the internal stresses in the sample after straining. Makar and Tanner (2000) analyzed the effect of plastic deformation and residual stress on the relative magnetic

permeability μ and magnetostriction of steels. Magnetostrictive measurements suggested that residual stresses do not play a major role in the variation of magnetic properties. The changes in the magnetic behavior were mainly attributed to the generation of pinning sites during the plastic deformation process.

More recently, some authors explored the impact of plasticity by comparing the magnetic behavior of plasticized materials in the loaded and unloaded states. El Youssef et al. (2020) showed that the application of tensile stress on prestrained non oriented Iron–Silicon samples resulted in a reduction of the deterioration caused by plastic strain until a characteristic stress value is attained. Above this threshold, the magnetic behavior deteriorates again. Leuning et al. (2018) studied the mechanisms of uniaxial plastic and elastic deformation on Iron–Silicon steel. It was concluded that after removal of the external loading, local compressive stress distributions were formed. Reloading the material led to an improvement of the magnetic properties. Regarding losses, Daem et al. (2020) showed that the large increase in energy losses of non-oriented steel after plastic straining was related to the increase in dislocation density. Hysteresis and losses, however, were strongly decreased by applying a reloading stress on the plasticized material. Iordache et al. (2003b,a) studied the effect of elastic and plastic tensile strain on the magnetic behavior of non oriented Iron–Silicon steel. The evolutions of μ, H_c, and Barkhausen noise energy in the loaded and corresponding unloaded states were reported, attesting the influence of both long-range internal stresses and dislocation density on the magnetic degradation associated with mechanical hardening. Hubert and Lazreg (2017) conducted experiments on a plastically deformed dual-phase steel (0.1, 1, and 3%). Anhysteretic magnetization and magnetostriction curves of plasticized samples obtained with or without applying stress were reported. A clear relationship was established between kinematic hardening and magnetic behavior in the case of uniaxial tensile stress. The validity of this approach has been recently confirmed through an experimental study on a Carbon steel (Maazaz et al., 2021).

All these studies confirm the strong coupling between elasticity, plasticity, and magnetic behavior, although there is no clear consensus on the origins of the effect of plasticity on the magnetic behavior. The effects of plasticity being sensitive on both hysteretic and anhysteretic behavior, it is likely that both the multiplication of pinning sites and the development of internal stresses play a significant role in magneto-plastic behavior.

On the modeling side, it is noticeable that only few magneto-elasto-plastic approaches are available. It should also be mentioned that most of them are one-dimensional, considering stress as a scalar, which makes them difficult to use for the modeling of practical electromagnetic systems, where stress is essentially multiaxial. Sablik (2001) and Sablik et al. (2004) modified the Jiles–Atherton model to take into account the change in the dislocation density N_d due to plastic deformation, and its effects on the hysteretic magnetic properties. Recently, a finite element modeling of punching was developed introducing a dependence in N_d in the parameters of the anhysteretic Sablik model (M'zali et al., 2020). Hug et al. (1997) and Hubert and Hug (1995) established an empirical relationship between plastic strain and magnetic properties to predict the plasticity induced changes on first magnetization curves, core losses, and coercive field for a non-oriented Iron–Silicon sheet. Hubert et al. (2005) and Hubert and Daniel (2006) later combined a micromechanical modeling of the plastic hardening with a magneto-elastic multiscale model in order to reproduce the influence of small plastic strains (<1%) on the anhysteretic magnetic and magnetostrictive behavior of a ferromagnetic polycrystal. In this approach, plastic strain is treated through the resulting residual stress field. Shi (2020) proposed a magneto-elasto-plastic coupling model for ferromagnetic materials. Applied magnetic field, applied stress, and plastic deformation were considered using an equivalent field method. Modeling results separated the effect of plastic strain and reloading stress. No comparison with experimental results were shown for plasticized samples. Hubert and Lazreg (2017) have also proposed a macroscopic approach using the kinematic hardening parameters to model the same phenomenon. The relationship between kinematic hardening and residual stress was discussed considering a plastic strained material as a two phase system. Effects of reloading stress and three levels of plastic strain (up to 3%) on magnetization and magnetostriction curves were modeled, and compared to experimental results.

The coupling between plasticity and magnetic behavior is then usually modeled considering two effects: the evolution of the dislocation density and the development of internal stresses. The effect of reloading stress has been limited so far to low levels of plastic strain, using magneto-elastic approaches. The modeling of the interaction between plasticity and magneto-elastic effects hence remains an open path, particularly at high plastic strain levels.

This work reports a thorough magneto-mechanical characterization of a high formability electrical steel (DC04, produced by ArcelorMittal) subjected to various plastic strain levels, from low levels to necking. A three-dimensional multiscale modeling for the magneto-mechanical behavior of elastically and plastically strained samples is then proposed. This modeling approach is the first to combine both the effect of internal stresses resulting from plasticity and the effect of the evolution of the dislocation density in order to predict the magneto-elastic properties of plastically deformed materials. Modeling results are finally compared to experimental measurements.

2. Experimental characterization of the magneto-mechanical behavior

This section is dedicated to the experimental characterization of the magneto-mechanical behavior of DC04. The experimental setup is first presented. The mechanical behavior of the material is then characterized and the mechanical hardening process is discussed. The magnetic characterization (major loops and anhysteretic curves) obtained for different levels of elastic and plastic deformation are then presented. The effects of mechanical reloading on the magnetic behavior of plasticized material are presented.

2.1. Magneto-mechanical characterization setup

The characterization setup is presented in Fig. 1. It is designed to measure the magnetic induction B and the longitudinal total strain of a ferromagnetic materials subjected simultaneously to a magnetic field H and a uniaxial mechanical stress σ_u, in the direction of the applied magnetic field (direction **x**, defined in Fig. 1). Fig. 2 shows a general view of the setup.

A tension–compression machine (Zwick/Roell Z030), connected to a computer, is used to apply a force F along direction **x**. Classical jaws grip the sample. The force F is measured and controlled using a 30 kN load cell (Xforce P). The measurement accuracy of this sensor is about ±0.15%. The level of measured noise is ±2 N (one standard deviation).

The longitudinal engineering strain $\varepsilon_{//}^{\text{eng}}$ is obtained from a strain gauge connected to a strain gauge conditioner–amplifier (Vishay 2120B). Details on the strain measurement are given in Appendix A. From the evaluation of $\varepsilon_{//}^{\text{eng}}$, the true longitudinal strain $\varepsilon_{//}$ is classically calculated using (1).

$$\varepsilon_{//} = \ln(1 + \varepsilon_{//}^{\text{eng}}) \tag{1}$$

The longitudinal (true) plastic strain ε_p is defined as the total longitudinal strain remaining after unloading. For each level of plastic strain, the cross-section S of the sample is measured after unloading. Neglecting the elastic strain compared to the plastic strain, the true (or Cauchy) stress σ_u is evaluated using (2). The measurement error on S is estimated at ±0.3% (see Appendix B).

$$\sigma_u = \frac{F}{S(\varepsilon_p)} \tag{2}$$

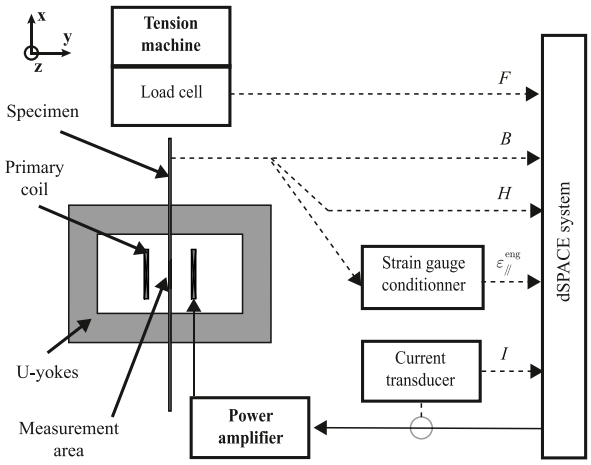

Fig. 1. Magneto-mechanical characterization rig, measurement setup, and representation of coordinate system.

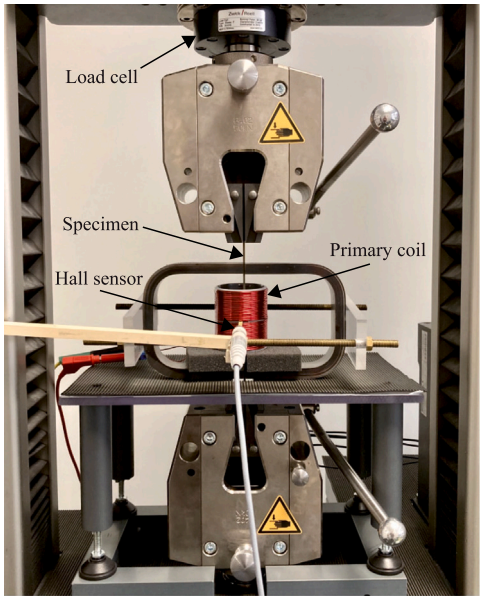

Fig. 2. General view of the characterization setup.

The magnetic circuit, constituted of two U-shaped Iron–Silicon yokes, ensures the closure of the magnetic field generated by a primary coil (50 turns of 16 AWG wire), powered by a power amplifier (Kepco 72-14MG). The current I is measured using a LA 125-P current transducer.

The magnetic field H is measured using a GM08 Gaussmeter and a transverse Hall probe. This sensor can measure H from DC to 10 kHz with a ±1% accuracy. The measured noise level is ±35 A m^{-1} (one standard deviation).

The electromotive force e induced in a secondary winding (N = 80 turns in this case) wound around the sample is evaluated in real-time. The variation of magnetic induction δB is calculated from the numerical integration of $e(t)$ following the classical relationship (3).

$$\delta B(t) = \frac{1}{N S(\varepsilon_p)} \int_0^t e(t)\,\mathrm{d}t \tag{3}$$

The measured noise level is evaluated at 0.1 mT, and the drift on δB always remains below 0.5 mT/s. The error on the measurement of $S(\varepsilon_p)$ (see Appendix B) is taken into account in the evaluation of δB. The reference state for the evaluation of B is the demagnetized state. The description of the demagnetization process and minimization of the drift are detailed in Domenjoud et al. (2019).

The measurement of B is very reproducible with a reproducibility error close to 0.2%. Conversely, the reproducibility error is evaluated close to ±1% for the measurement of H. This is explained by the difficulty to place the active element of the Hall probe in the same position all along the tests. Tests conducted under stress show that these errors are independent of the mechanical state of the material. These errors are taken into account in the presentation of the results.

The measurement acquisition, the generation of the excitation signal (including control loop feedback of the current) are ensured by a DS 1006 dSPACE processor board at a sampling frequency of 50 kHz. More details on the setup can be found in Domenjoud et al. (2019).

The samples studied in this work are made of polycrystalline low Carbon steel (DC04) produced by ArcelorMittal (1996). No heat treatment is applied to the specimens. The dimensions of the samples (250 mm × 20 mm × 2 mm) ensure the homogeneity of magnetic field and mechanical stress in the measurement area. The samples were obtained from larger steel sheets by electroerosion machining in order to minimize the residual stresses induced by the cutting procedure. Several samples have been tested, in a limited number of configurations, to evaluate the reproducibility of the measurements. Results presented in Sections 2.2 and 2.3 have been obtained on a single sample, and include the errorbars representative for the reproducibility error.

2.2. Mechanical characterization of DC04

Fig. 3 shows the mechanical behavior of DC04, at room temperature, up to 22% strain, just before the necking region ($\varepsilon_p^n = 23\%$). From the virgin state, the sample was subjected to loading–unloading cycles of increasing stress amplitude by steps of 25 MPa. Until 100 MPa, the remnant strain ε_p after unloading was negligible. It became significant from 125 MPa ($\varepsilon_p = 0.005\%$). Young modulus Y and Yield stress R_e are estimated close to 200 GPa and 120 MPa, respectively. In the plastic regime, a time relaxation varying from a few minutes up to one hour has been respected to reach the total relaxation of the strain at constant stress (El Youssef et al., 2020; Iordache et al., 2003a). The material is then in a stabilized mechanical state. The material is then unloaded, and the plastic strain ε_p is evaluated. Three strain gauges have been glued successively to cover the full elongation range (see Appendix A). Twelve levels of plastic deformation ε_p were identified: 0.017, 0.045, 0.073, 0.142, 0.258, 0.491, 1.04, 2.67, 5.22, 8.47, 14.5, and 21.7%. This wide range of plastic strain levels allows to cover the tensile stress curve up to necking, as required for plastic forming processes. For each value of ε_p, the material was characterized again after the application of a uniaxial elastic reloading stress σ_u of 50, 100 MPa and $\sigma_u^{\max}$. $\sigma_u^{\max}$ is the maximum stress value reached before the unloading. The magneto-elastic response and the identified mechanical parameters are consistent with the literature (ArcelorMittal, 1996; Ledoux et al., 2010; Niechajowicz, 2010).

As expected, the slope of the loading–unloading curves was always very close to the Young modulus Y of the virgin material. No Lüder's plateau was observed between the elastic and the plastic regime. As a consequence, the homogeneous strain-hardening domain starts from a stress value close to R_e.

The reproducibility of these measurements has been evaluated by comparing the mechanical states obtained under stress with those obtained during preliminary tests on other samples. The variations of stress amplitude σ_u observed for each value of the longitudinal strain $\varepsilon_{//}$ were about ±1%, while the variations of $\varepsilon_{//}$ for each value of σ_u were about ±4%. This variability can be explained by some heterogeneity in the samples leading to small variations in the stabilized states reached under stress. These reproducibility errors are taken into account in the description of the results.

Evolution of hardening stress ($\sigma_u - R_e$) and strain-hardening rate θ (defined as $\Delta\sigma_u/\Delta\varepsilon_p$ and positioned at the mean values of two consecutive values of ε_p) are represented in Fig. 4 as a function of ε_p, in

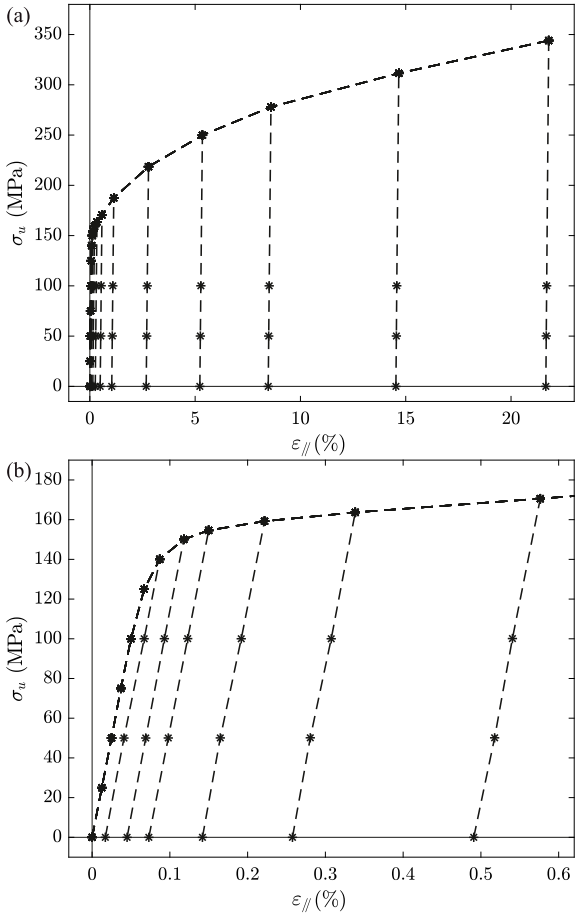

Fig. 3. Tensile curve of DC04 (stabilized mechanical states) : (b) is a zoom of the full curve (a) in the low strain region.

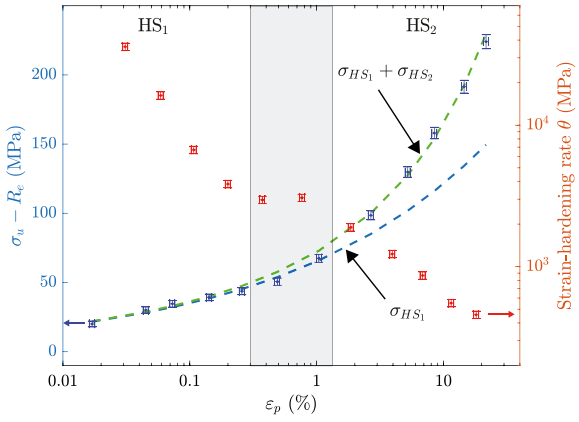

Fig. 4. Evolution of the hardening stress ($\sigma_u - R_e$) in the stabilized state and strain-hardening rate θ of DC04 as a function of tensile plastic strain ε_p. The figure shows two stages of hardening, named HS$_1$ and HS$_2$. The identified Ludwik laws are shown in dashed lines. The transition zone between HS$_1$ and HS$_2$ is shown in gray. (For interpretation of the references to color in this figure legend, the reader is referred to the web version of this article.)

logarithm scale. As classically observed in metals (Kuhlmann-Wilsdorf, 1985), the strain-hardening rate is high at the beginning of the plastic regime and decreases as ε_p increases. Two hardening stages HS$_1$ and HS$_2$ are observed, with a transition zone in the vicinity of 1% of ε_p, characterized by an almost constant strain-hardening rate. A simple and widely used approach to describe the metal strain-hardening curve is

Table 2
Elastic (left) and plastic (right) parameters for DC04 identified from the tensile test.

Parameter	Y	R_e	K_1	K_2	m_1	m_2	ε_p^n
Value	200 10^9	120 10^6	226 10^6	273 10^6	0.270	0.803	0.23
Unit	Pa	Pa	Pa	Pa	–	–	–

the power law of Ludwik (1909) that relates the applied stress σ_u to R_e and ε_p (4).

$$\sigma_u = R_e + K\,{\varepsilon_p}^m \tag{4}$$

K is the resistance coefficient and m the hardening coefficient. These parameters can be obtained from the linear regression of the logarithmic representation of σ_u as a function of ε_p. As discussed in Li et al. (2016), a two-stage hardening behavior cannot be represented by a single power law relationship. A Ludwik law for σ_{HS_1} in the first hardening stage has been identified first in the low strain region, resulting in (5).

$$\sigma_{HS_1} = K_1\,{\varepsilon_p}^{m_1} \tag{5}$$

with $K_1 = 226$ MPa and $m_1 = 0.270$. The result is shown as a blue dashed line in Fig. 4. From the difference between measured values and σ_{HS_1} during HS$_2$, a second Ludwik law for σ_{HS_2} is superimposed to σ_{HS_1}. A linear regression of this difference in the high strain region is used to obtain the parameter for this second term (6).

$$\sigma_{HS_2} = K_2\,{\varepsilon_p}^{m_2} \tag{6}$$

with $K_2 = 273$ MPa and $m_2 = 0.803$. This second power term is representative of the second hardening stage (HS$_2$) starting close to 1% plastic strain. Finally, the modified Ludwik law (7) is used to describe the mechanical behavior of the material.

$$\sigma_u = R_e + K_1\,{\varepsilon_p}^{m_1} + K_2\,{\varepsilon_p}^{m_2} \tag{7}$$

This modified Ludwik law is shown as a green dashed line in Fig. 4. The mechanical material parameters are summarized in Table 2.

This two-stage hardening is commonly interpreted as the result of two distinct mechanisms (Degauque, 1993; Lemaitre and Chaboche, 1994; Feaugas, 1999; Hubert et al., 1999; Kleber and Vincent, 2004; Callister and Rethwisch, 2014). In the first stage of plasticity (HS$_1$), the dislocation density N_d increases in a fairly homogeneous fashion within grains, and intergranular internal stress appears. This internal stress component is associated with the grain-boundary structure, i.e. with the mechanical incompatibilities between grains. From this stage, N_d keeps increasing with ε_p, clusters are formed, arrange in bundles and then in cells, producing heterogeneous structures of dislocations. The transition between HS$_1$ and HS$_2$ is connected to the appearance of a heterogeneous structure of dislocations, which promotes a decrease of the intergranular stresses and the appearance of significant intragranular stresses (Feaugas, 1999).

Based on X-ray techniques and transmission electron microscopy, further works have investigated the evolution of internal stresses and dislocation structure in plasticized materials (Ashby, 1970; Astie et al., 1981; Feaugas, 1999; Hubert et al., 1999; Hug et al., 2002; Daem et al., 2020). Long-range stress fields appear to control the hardening process within the first percents of plastic straining (HS$_1$). In the meantime, a very weak increase of the dislocation density was observed. At higher levels of ε_p (HS$_2$), the evolution of internal stress is reduced, and the hardening process is more controlled by short-range interactions between moving dislocations and the steadily increasing density of geometrically-necessary dislocations.

2.3. Magneto-mechanical characterization of DC04

Magnetization is the result of nonlinear reversible and irreversible mechanisms. Considering quasi-static processes, the irreversible contribution arises from the pinning/unpinning of domain walls on defects in

the material (Bertotti, 1998). This mechanism is dissipative, responsible for the typical $B-H$ hysteresis loop observed in magnetic materials. The reversible part corresponds to the so-called anhysteretic behavior, that describes the minimum energy state of a material under a given external loading (Bozorth, 1951; Gourdin et al., 1998). This state can be obtained in a sample by applying a decaying alternative field superimposed to a DC component (see Bozorth (1951), Jiles (1991), Fiorillo (2004) and Daniel and Domenjoud (2021) and Appendix C).

For each level of ε_p and σ_u (shown by markers in Fig. 3), major $B-H$ loops and anhysteretic $B_{anh}-H_{anh}$ measurements are conducted. Three major loops reaching maximum magnetic field $\pm H_{max}$ (about ± 3.8 kA m^{-1}) are measured at 1 Hz frequency (quasi-static process). 5000 points are recorded on each loop, and a moving average of 30 points is applied on H measurement. The anhysteretic process and the details on the evaluation of anhysteretic values H_{anh} and B_{anh} of the magnetic field and magnetic induction, respectively, are described in Appendix C. Anhysteretic magnetization curves (30 points each) are evaluated for positive values of H_{anh}.

Remnant induction B_r, magnetic induction $B_{H_{max}}$ at H_{max}, coercive field H_c and relative anhysteretic magnetic permeability μ_{anh} are extracted from major loops and anhysteretic measurements. B_r and H_c are evaluated from a linear regression (10 points) on the $B(H)$ curve at $H=0$ and $B=0$, respectively. An average of the six values obtained for the three major loops is applied. $B_{H_{max}}$ is evaluated from a linear regression on B around $H=3.6$ kA m^{-1}. A secant definition (8) is used for the anhysteretic permeability μ_{anh}.

$$\mu_{anh} = \frac{1}{\mu_0}\frac{B_{anh}}{H_{anh}} \tag{8}$$

where μ_0 is the vacuum magnetic permeability.

2.3.1. Influence of plastic deformation under no applied stress

Figs. 5(a) and 5(b) show the magnetic hysteresis loops and anhysteretic behavior of DC04 for different levels of ε_p from no plastic deformation up to the maximum value (21.7%), without applied external stress (unloaded state).

The increasing plastic strain levels lead to a nonlinear degradation of the hysteretic and anhysteretic behaviors. This degradation is particularly sharp at low plasticity levels ($\varepsilon_p < 0.5\%$). Besides, a bulging of the loop at H_c is observed at high levels of ε_p. For a given value of H, B decreases as ε_p increases. The amplitude of this drop varies depending on the level of H and is especially significant in the low and medium magnetic field region.

From a micromagnetic viewpoint, the first part of the magnetization curves is mostly controlled by domain wall motions, while the second part, beyond the knee of the magnetization curve, involves the coherent rotation of elementary magnetic moments in the magnetic domains (Jiles, 1991; Fiorillo, 2004). Fig. 5 shows that plasticity strongly affects the magnetic behavior at low and medium magnetic field. Conversely, the sensitivity to ε_p is reduced at high field. Consequently, it can be inferred that plasticity has a larger influence on domain wall motion than on the magnetization rotation mechanism.

However, since the effect of plasticity is also observed on the anhysteretic behavior (Fig. 5(b)), which is insensitive to pinning/unpinning mechanisms, it is clear that the impact of plasticity on the magneto-mechanical behavior cannot be reduced to the multiplication of the pinning sites. The effect of plasticity on the reversible part of the behavior can be partly interpreted as a magneto-elastic effect related to the internal stresses developing with plasticity (Hug et al., 1996; Hubert et al., 1999; Iordache et al., 2003b; Hubert and Lazreg, 2017; Stupakov et al., 2007). It can be modeled using a stress tensor representative for the internal back stresses affecting the larger volume of the material. The results shown in Fig. 5 regarding a tensile plastic strain are consistent with an overall compressive internal stress, as already noticed by other authors (Cullity, 1972; Abuku, 1977; Gatelier-Rothea et al., 1998; Kleber and Vincent, 2004).

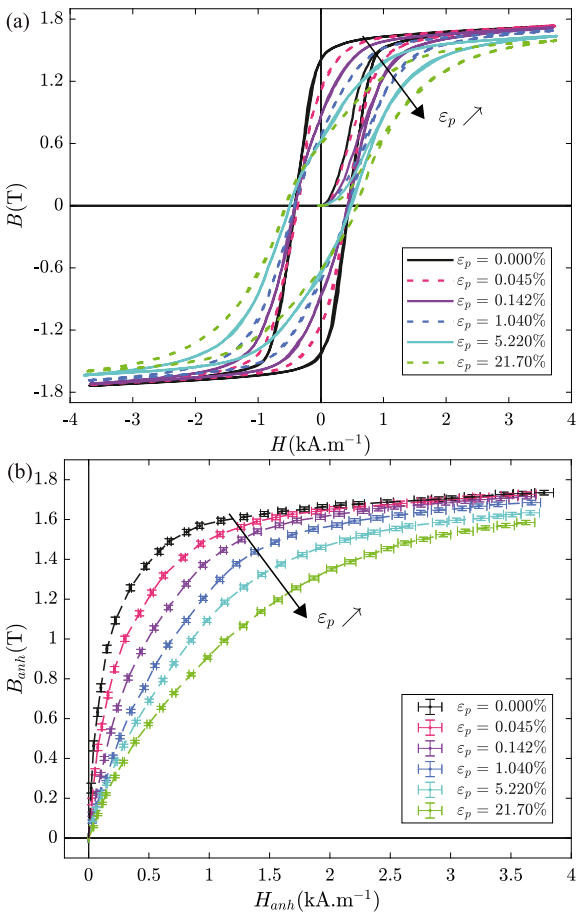

Fig. 5. Hysteresis loops (a) and anhysteretic behavior (b) of DC04 under different levels of tensile plastic strain ε_p, for the unloaded state ($\sigma_u = 0$).

Magnetic parameters B_r, $B_{H_{max}}$ and H_c in the unloaded state, extracted from Fig. 5(a), are plotted in Fig. 6, as functions of ε_p (logarithmic scale). The regions identified as HS_1 and HS_2 have also been reported. The maximum induction $B_{H_{max}}$ (at maximum applied field H_{max}) decreases slowly as ε_p increases, indicating that the material requires a greater value of H to reach the initial value of $B_{H_{max}}$ (at $\varepsilon_p = 0$). The saturation magnetization is a material constant, unaffected by stress or pinning effects. Magnetization curves are hence expected to converge to the saturation limit, whatever the level of ε_p, but saturation is reached for values of H that increase nonlinearly with ε_p, explaining this evolution of $B_{H_{max}}$. The significant variations of B_r and H_c induced by plasticity seem to correlate with the two hardening stages HS_1 and HS_2. B_r decreases sharply in HS_1, and then the evolution saturates beyond the transition stage. Because of the accuracy of the magnetic field measurement, the evolutions of H_c are more uncertain but H_c seems to increase weakly during HS_1, and then sharply during HS_2. These observations are consistent with results from the literature (Hug et al., 1997, 2002; Landgraf et al., 2020; Daem et al., 2020) and provide grounds to explain the increase of core losses due to plastic deformation.

Remnant induction B_r and coercive field H_c are usual indicators of hysteresis in magnetic materials and can be used to analyze the dissipation mechanisms. B_r is mainly controlled by 90° domain wall motions (motions of walls between domains with perpendicular magnetization), while H_c is more connected to 180° domain wall motions (motions of walls between domains with antiparallel magnetization) (Jiles, 1991). Fig. 6 shows that B_r is very sensitive to ε_p during HS_1, while H_c is more affected during HS_2. As previously discussed, the development of

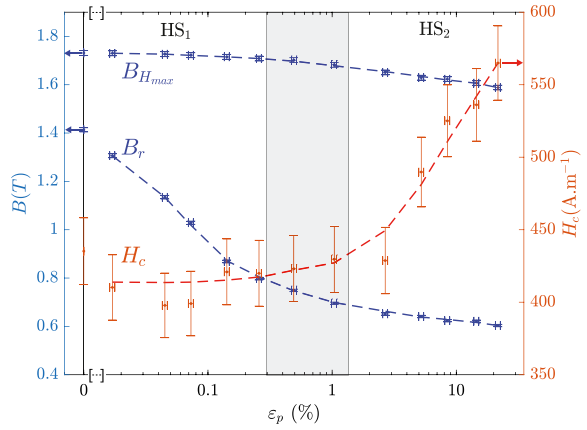

Fig. 6. Remnant induction B_r, maximum induction $B_{H_{max}}$ and coercive field H_c versus tensile plastic strain ε_p, for the unloaded state ($\sigma_u = 0$). The transition region between HS_1 and HS_2 is shown in gray. The dashed lines are guides for the eye.

internal stresses (HS_1) and the fast multiplication of pinning sites (HS_2) are the two main mechanisms for the interpretation of magneto-plastic couplings. These mechanisms can serve as a basis for the interpretation of Fig. 6. In HS_1, the internal compressive stress favors the presence of 90° domains (magneto-elastic effect for positive magnetostriction materials). The increase in the population of transverse domains with ε_p (corresponding to an increase in the level of internal compressive stress) induces that, for a given magnetic field, lower magnetization is achieved than in the case of an unstressed specimen. This effect saturates as the level of internal stress stabilizes, explaining the evolution of B_r with ε_p in Fig. 6. Conversely, H_c is commonly associated with the pinning of domains (either 90° or 180°) on the defects within the material. Initially, isolated dislocations create little perturbation on domain wall motion, but as their number steadily increases during HS_1, H_c slightly increases. When reaching HS_2, tangles start to form. Not only these dislocations structures represent a much more significant obstacle to domain wall motion, but they also contribute to fuel the increase of the dislocation density N_d. This mechanism explains the sharp increase of H_c during HS_2. An evolution law of H_c in $\sqrt{N_d}$ is often found in the literature (Seeger et al., 1964; Qureshi and Chaudhary, 1970; Lubitz, 1974; Astie et al., 1981). As a summary, the evolution of the magnetic parameters are mostly attributed to long-range internal stress effects during HS_1 and to the formation of dislocation structures with a strong increase in N_d during HS_2.

Fig. 7(a) shows the anhysteretic magnetic permeability μ_{anh}, at different values of the magnetic field H_{anh}, as a function of the tensile plastic strain ε_p, in the unloaded state. Similarly, Fig. 7(b) plots μ_{anh}, at different levels of ε_p, as a function of H_{anh}. As already observed in Fig. 5(b), plasticity strongly damages μ_{anh}, from the early stages of plasticity. This degradation tends to saturate from around 0.3% ε_p, at the transition between the two hardening stages HS_1 and HS_2. Also, the sensitivity to plastic deformation nonlinearly depends on the value of H_{anh}. Values of μ_{anh} evaluated at low and medium magnetic field are more sensitive to the plasticity than the values obtained at higher values of H_{anh}, closer to saturation. This is expected since the saturation state is a material characteristic and is not supposed to be sensitive to plasticity. Moreover, the decrease of μ_{anh} as a function of H_{anh} is slighter as the material is highly plasticized, which is due to the already low values of μ_{anh} on highly plasticized materials (the hysteresis loop slants).

The evolution of μ_{anh} is consistent with the interpretation made regarding the mechanisms at play during HS_1 and HS_2. At low levels of plastic strain (HS_1), the effect of plasticity is mainly controlled by the development of internal compressive stresses. A higher field H_{anh}

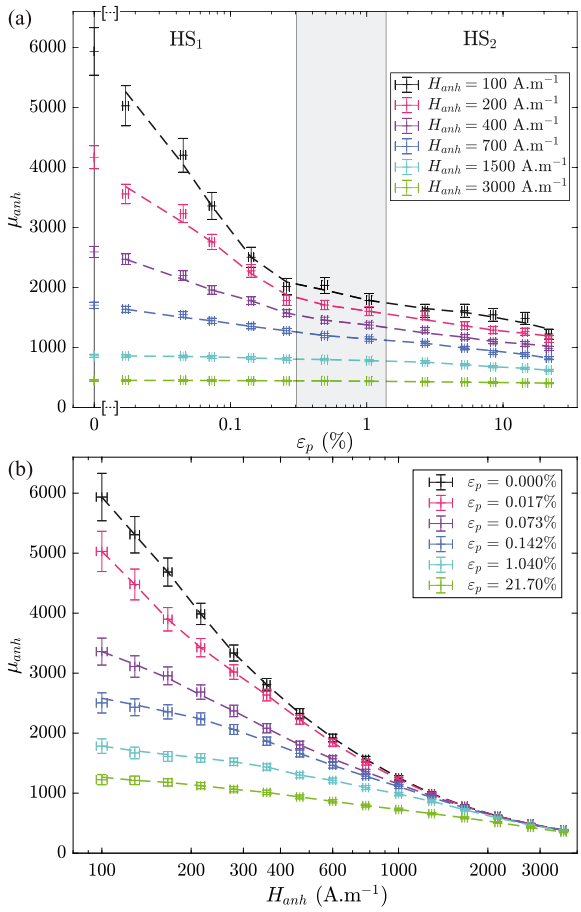

Fig. 7. Anhysteretic magnetic permeability μ_{anh} in the unloaded state ($\sigma_u = 0$) versus tensile plastic strain ε_p (a) and magnetic field H_{anh} (b), respectively. The transition region between HS_1 and HS_2 is shown in gray. The dashed lines are guides for the eye.

is required to reach a given value of B_{anh}, so that μ_{anh} monotonically decreases with ε_p. During HS_2, the effect of plasticity on the permeability is moderate, which is consistent with the saturation of the internal stress and the formation of dislocation structures, which affects mostly the dissipation mechanisms, and much less the anhysteretic parameters. As evident from Fig. 7(b), for each level of ε_p, μ_{anh} converges towards very small values near H_{max}. μ_{anh} then becomes almost insensitive to the level of plastic deformation. However, as highlighted in previous works (Seeger et al., 1964; Qureshi and Chaudhary, 1970; Lubitz, 1974; Degauque, 1993), plasticity has a strong effect on the initial susceptibility (χ_i), that evolves proportionally to $1/\sqrt{N_d}$. This suggests that the decrease of μ_{anh} in HS_2 can also be connected to the increase of the dislocation density.

2.3.2. Influence of elastic reloading stress

This section deals with the effect of a reloading tensile stress σ_u on the magneto-mechanical behavior of DC04 samples plasticized in tension at various levels (as shown in Fig. 3). After reaching a given tension stress $\sigma_u = \sigma_u^{max}$, the material is unloaded, and then reloaded again in tension with amplitudes σ_u of 50 MPa, 100 MPa and σ_u^{max}. This way, the reloading process is elastic and the dislocation structure is assumed to be unchanged compared to the unloaded state.

Fig. 8 shows the hysteresis loops and anhysteretic curves under four levels of reloading stress σ_u (0, 50 MPa, 100 MPa and σ_u^{max}). The results are shown for three levels of plastic strain ε_p: 0.017, 1.040 and 21.70%. These figures show that the sensitivity of the magnetic behavior to a reloading stress highly depends on the plasticized state of the material.

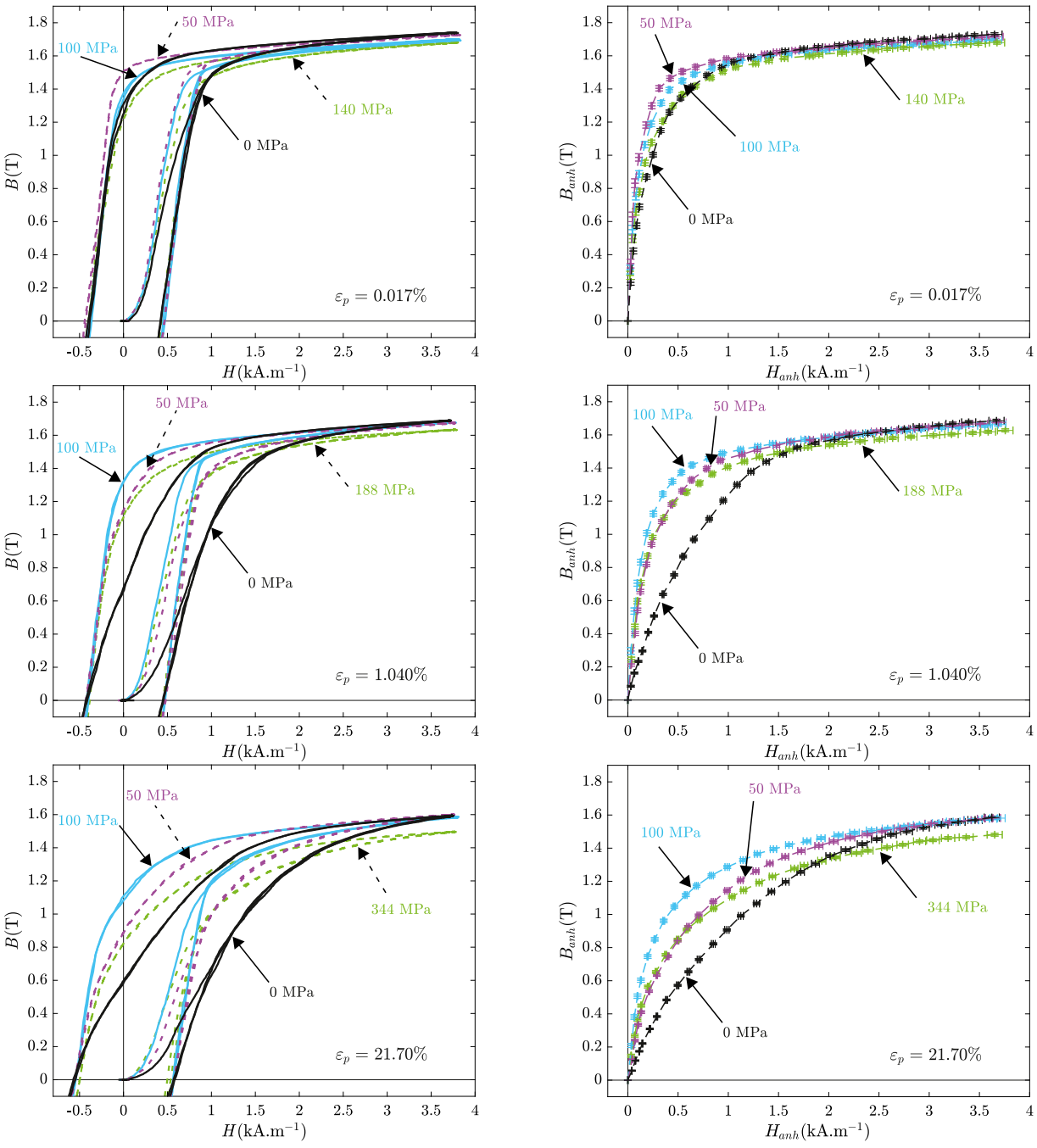

Fig. 8. Hysteresis loops (left) and anhysteretic curves (right) of DC04, at different levels of reloading stress σ_u (0, 50 MPa, 100 MPa and $\sigma_u^{\max}$) and for three different levels of tensile plastic strain ε_p (0.017, 1.040 and 21.70% from top to bottom).

At low magnetic field, whatever the level of ε_p, the reloading stress σ_u induces first an increase of induction, followed by a decrease at higher stress values. The effect is reversed at high magnetic field (a decrease in induction followed by an increase), which is characteristic of the Villari effect (or Villari reversal), classically observed in Iron based materials (Villari, 1865; Cullity, 1972; Daniel et al., 2008). This effect is also evident from the crossover between the magnetization curves for different stress levels. It can be seen that a moderate reloading stress allows a partial recovery, at low field, of the behavior of the virgin (not plasticized) material.

The magnetic parameters H_c, $B_{H_{max}}$ and B_r have been extracted from all hysteresis measurements. H_c appears to be almost unaffected by the application of the reloading stress σ_u apart from a slight monotonic decrease. The data are therefore not presented here. The results for $B_{H_{max}}$ and B_r are shown in Fig. 9. $B_{H_{max}}$ decreases slightly and monotonically as a function of σ_u whatever the level of ε_p. Conversely, B_r first increases (partial recovery) and then decreases when increasing σ_u. In the virgin state ($\varepsilon_p = 0$), the value of σ_u for which B_r is maximum is close to 50 MPa. This value seems to gradually increase as ε_p increases. These evolutions are consistent with the decrease of core losses induced by reloading stress as observed in Daem et al. (2020).

The anhysteretic permeability μ_{anh} has been evaluated for each mechanical state and is shown in Figs. 10(a) and 10(b) for H_{anh} equal to 250 and 1250 A m^{-1}, respectively. These figures show that μ_{anh} first increases and then decreases with σ_u. In the virgin state, the value σ_u^r of σ_u for which μ_{anh} is maximum is close to 50 MPa. As observed for B_r, this optimum stress value that provides maximum permeability seems to increase as ε_p increases.

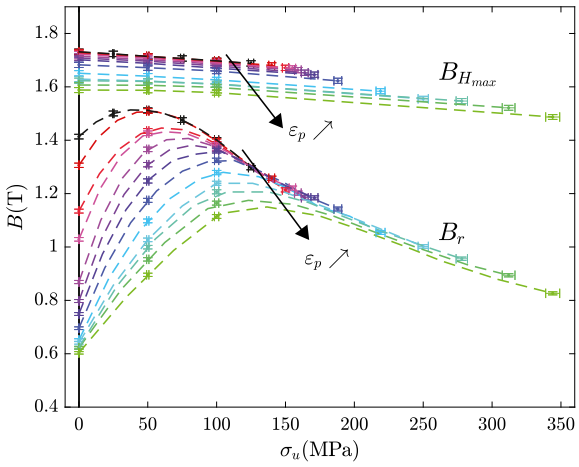

Fig. 9. Maximum induction $B_{H_{max}}$ and remnant induction B_r as a function of the reloading stress σ_u for several levels of tensile plastic strain ε_p (from 0 to 21.7% as described in Fig. 3). The dashed lines are guides for the eye.

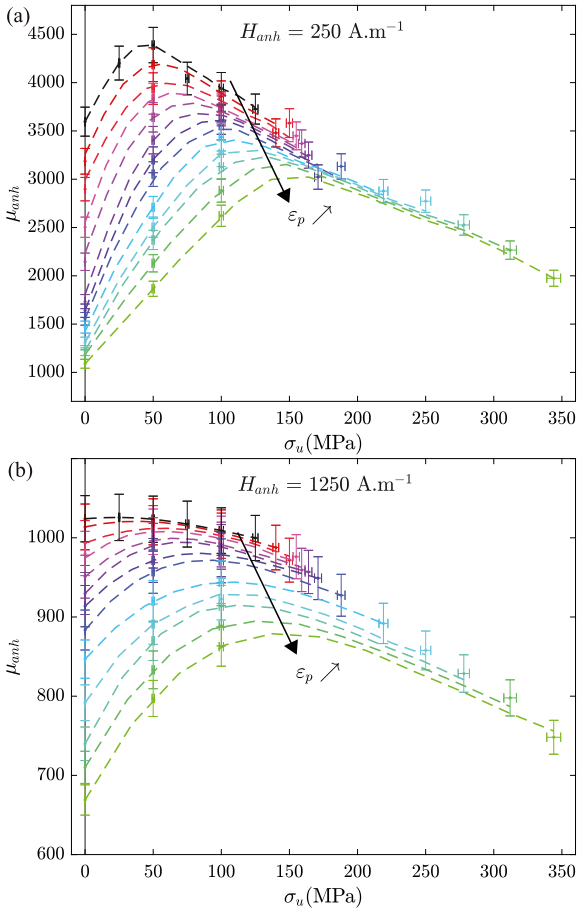

Fig. 10. Anhysteretic magnetic permeability μ_{anh} at H_{anh} = 250 A m^{-1} (a) and H_{anh} = 1250 A m^{-1} (b) as a function of the applied uniaxial stress σ_u for DC04 samples plasticized at several levels of plastic strain ε_p (from 0 to 21.7% as described in Fig. 3). The dashed lines are guides for the eye.

The non-monotonic evolution of B_r and μ_{anh} with respect to the applied stress amplitude is a known magneto-elastic effect already observed in Iron–Silicon steel (Daniel et al., 2014; Perevertov, 2017; Hubert, 2019), mild steel (Craik and Wood, 1970) and dual-phase steel (Hubert and Lazreg, 2017). Daniel et al. (2014) interpreted it as an effect of stress on the initial domain configuration: under high uniaxial tension, domains oriented in the direction of the applied stress are dominant, creating additional local demagnetizing fields that counter balance the positive effect of tension on the magnetic permeability. In a similar way, Perevertov (2017) considered that demagnetizing fields are generated at grain boundaries and material surface due to the suppression of transverse closure domains induced by tension stress. Hubert (2019) recently proposed to model this peculiar effect by the introduction of second-order magnetostriction terms in an energy based approach.

The following section is dedicated to the modeling of the magneto-elasto-plastic behavior presented in this section.

3. Modeling of the magneto-mechanical behavior

This section is dedicated to a multiscale approach for the modeling of the magneto-elasto-plastic behavior of DC04. The proposed modeling tool is based on multiscale approaches for magneto-elastic behavior (Daniel et al., 2004, 2008, 2014) and more particularly on a simplified version (Daniel et al., 2015; Bernard and Daniel, 2015) allowing an easy implementation for structural analysis. Following the proposal of Hubert (2019), Hubert et al. (2022) and Zhao et al. (2021), a second-order stress term is introduced in the magneto-elastic energy to describe the non-monotonic evolution of the magnetic behavior under stress. An extension to magneto-plastic behavior is then proposed incorporating both the effect of internal back stress and the evolution of the dislocation density during the plasticity process. Finally, a phenomenological description of the coercive field and remnant induction as a function of stress and plastic strain is provided to include the dissipation effects. This combination of modeling approaches provides for the first time a comprehensive model for the magneto-elasto-plastic behavior of ferromagnetic materials.

The multiscale approach, in its simplified version (Daniel et al., 2015), is first described followed by its extension to include plasticity effects. The identification of the key parameters for the magneto-elasto-plastic behavior is then discussed and a methodology is presented. Finally, a description of magnetic dissipation parameters is proposed based on existing phenomenological modeling approaches.

3.1. Simplified anhysteretic multiscale approach

In the simplified version of the multiscale model (Daniel et al., 2015), the polycrystalline material is described as a fictitious single crystal with a very large number of easy magnetization directions. The material is therefore treated as a collection of magnetic domains randomly oriented. As a consequence, and contrarily to the full multiscale approach (Daniel et al., 2008, 2014), the influence of stress on the rotation mechanism (leading to the Villari reversal) is not taken into account.

The local magnetization $\mathbf{M}_\alpha$ (9), in a domain α, is fully defined by its orientation $\boldsymbol{\alpha}$ (unit vector defined by the direction cosines α_i of the magnetization) and the saturation magnetization M_{sat} of the material. Assuming an isotropic and isochoric magnetostrictive behavior, the local magnetostriction strain $\boldsymbol{\epsilon}_\alpha^\mu$ is given by (10), where λ_{sat} is the saturation magnetostriction of the material. $\otimes$ represents the tensor product and $\mathbf{I}$ is the second-order identity tensor.

$$\mathbf{M}_\alpha = M_{\text{sat}}\,\boldsymbol{\alpha} \tag{9}$$

$$\boldsymbol{\epsilon}_\alpha^\mu = \frac{3}{2}\lambda_{\text{sat}}\,\mathbf{S}_\alpha \tag{10}$$

with

$$\mathbf{S}_\alpha = \boldsymbol{\alpha}\otimes\boldsymbol{\alpha} - \frac{1}{3}\mathbf{I} \tag{11}$$

At the domain scale, the local free energy W_α (12) of the material is written as the sum of the anisotropy (W_α^{an}), magnetostatic (W_α^{mag}) and magneto-elastic (W_α^{el}) energies.

$$W_\alpha = W_\alpha^{\text{an}} + W_\alpha^{\text{mag}} + W_\alpha^{\text{el}} \tag{12}$$

The anisotropy energy W_α^{an} accounts for the existence of preferred orientations for the magnetization (macroscopic easy axes). Its expression is given in Daniel et al. (2015) in the case of uniaxial anisotropy. In the case of macroscopic isotropy, as assumed here, this term vanishes.

The magnetostatic (or Zeeman) energy W_α^{mag} (13) tends to favor domains with a magnetization $\mathbf{M}_\alpha$ close to the direction of the applied field $\mathbf{H}$ ($\mathbf{H} = H\mathbf{h}$). The symbol "·" denotes the scalar product.

$$W_\alpha^{\text{mag}} = -\mu_0\, \mathbf{H} \cdot \mathbf{M}_\alpha \tag{13}$$

The magnetoelastic energy W_α^{el} describes the effect of stress on magnetic behavior. Following the formulation developed by Hubert (2019), the magneto-elastic energy (14) is expressed as the sum of a first-order ($W_\alpha^{\text{el}(1)}$) and a second-order term ($W_\alpha^{\text{el}(2)}$).

$$W_\alpha^{\text{el}} = W_\alpha^{\text{el}(1)} + W_\alpha^{\text{el}(2)} \tag{14}$$

The first term (15) is the classical expression for the magneto-elastic energy introducing the stress tensor $\boldsymbol{\sigma}$ and the magnetostriction strain tensor $\boldsymbol{\epsilon}_\alpha^\mu$, where : is the double-dot product of the two second order tensors.

$$W_\alpha^{\text{el}(1)} = -\boldsymbol{\sigma} : \boldsymbol{\epsilon}_\alpha^\mu = -\frac{3}{2}\lambda_{\text{sat}}\, \mathbf{S}_\alpha : \boldsymbol{\sigma} \tag{15}$$

The second term (16) introduces a linear dependence of the magnetostriction tensor with stress allowing the description of the non-monotonic effect of stress on the magnetic permeability (Daniel et al., 2015; Hubert, 2019). In previous references following this approach (Hubert, 2019; Hubert et al., 2022; Zhao et al., 2021), the definition of $W_\alpha^{\text{el}(2)}$ introduces two second-rank stress-dependent tensors defined as a function of the applied stress. It implies the introduction of two additional material parameters whose physical meaning is not absolutely clear and whose identification can be tedious. We propose here to adopt a simplified definition by making use of the concept of deviatoric equivalent stress (Daniel and Hubert, 2010; Hubert and Daniel, 2011) introduced as a uniaxial stress into the second order term defined in Hubert (2019). $W_\alpha^{\text{el}(2)}$ is then defined by (16) with σ_{eq} the deviatoric equivalent stress defined by (17).[2]

$$W_\alpha^{\text{el}(2)} = -\frac{3}{2}\lambda'_{\text{sat}}\, \sigma_{\text{eq}}^2\, \mathbf{S}_\alpha : (\mathbf{h} \otimes \mathbf{h}) \tag{16}$$

$$\sigma_{\text{eq}} = \frac{3}{2}\, {}^t\mathbf{h} \left(\boldsymbol{\sigma} - \frac{1}{3}\text{tr}(\boldsymbol{\sigma})\mathbf{I}\right) \mathbf{h} \tag{17}$$

The definition of the magneto-elastic energy finally reduces to (18), introducing the isotropic second-order magnetostrictive constant λ'_{sat}.

$$W_\alpha^{\text{el}} = -\frac{3}{2}\, \mathbf{S}_\alpha \, : \left(\lambda_{\text{sat}}\, \boldsymbol{\sigma} + \lambda'_{\text{sat}}\, \sigma_{\text{eq}}^2\, (\mathbf{h} \otimes \mathbf{h})\right) \tag{18}$$

A better choice for the equivalent stress σ_{eq} may be made by adopting an equivalence criterion based on a second order definition of the elastic energy, probably leading to a slightly more complex definition of the magnetoelastic energy W_α^{el}. Moreover it can be shown (da Silva et al., 2022) that the constant λ'_{sat} can be defined as $\lambda'_{\text{sat}} = -\lambda_{\text{sat}}/2\sigma_u^r$ where σ_u^r is the characteristic value of the stress σ_u for which the permeability shows a change in monotonicity (in the virgin state $\epsilon_p = 0$). Such a relationship facilitates the identification of λ'_{sat}.

[2] It can be noticed that in the case of a uniaxial tension or compression stress applied parallel to the applied magnetic field, the equivalent stress σ_{eq} reduces to the amplitude of this uniaxial stress.

Once the local energy W_α is defined for any orientation, the volume fraction f_α of domains with orientation $\boldsymbol{\alpha}$ (19) is calculated as a function of the free energy according to a Boltzmann-type relation (Buiron et al., 1999; Daniel et al., 2008).

$$f_\alpha = \frac{\exp(-A_s\, W_\alpha)}{\int_{\boldsymbol{\alpha}} \exp(-A_s\, W_\alpha)\, \mathrm{d}\boldsymbol{\alpha}} \tag{19}$$

In this expression, A_s is a material parameter related to the initial susceptibility χ_i^0 of the unstressed anhysteretic magnetization curve (Daniel et al., 2008). It was shown to be defined as:

$$A_s = \frac{3\chi_i^0}{\mu_0\, {M_{\text{sat}}}^2} \tag{20}$$

Once f_α is known for any domain orientation, the macroscopic magnetization $\mathbf{M}$ (21) and magnetostriction $\boldsymbol{\epsilon}^\mu$ (22) are obtained through averaging operations over all directions.

$$\mathbf{M} = \langle \mathbf{M}_\alpha \rangle = \int_{\boldsymbol{\alpha}} f_\alpha\, \mathbf{M}_\alpha\, \mathrm{d}\boldsymbol{\alpha} \tag{21}$$

$$\boldsymbol{\epsilon}^\mu = \langle \boldsymbol{\epsilon}_\alpha^\mu \rangle = \int_{\boldsymbol{\alpha}} f_\alpha\, \boldsymbol{\epsilon}_\alpha^\mu\, \mathrm{d}\boldsymbol{\alpha} \tag{22}$$

From a practical point of view, a set of 34 635 directions distributed on nodes of a triangular mesh of an icosphere (a sphere built by regular subdivision of the triangular faces of an icosahedron) is used to describe the domain orientations (Daniel and Galopin, 2008; Bernard et al., 2019; Daniel et al., 2022).

3.2. Incorporation of plasticity effect

The effect of plasticity on the magneto-elastic behavior is introduced through two different mechanisms. The first mechanism is the introduction of the effect of internal stresses on the macroscopic behavior through the definition of an internal back stress $\boldsymbol{\sigma}_{int}$. The second is the introduction of a dependence of the macroscopic behavior on the level of plasticity through the dislocation density N_d.

3.2.1. Introduction of the internal back stress due to plastic straining

Neglecting a possible contribution of the isotropic hardening of the material, a macroscopic equivalent stress tensor $\boldsymbol{\sigma}_{int}$ representative for the internal stress state can be estimated from the kinematic hardening (Hubert and Lazreg, 2017; Maazaz et al., 2021). $\boldsymbol{\sigma}_{int}$ (23) shows the same symmetry as the plastic strain tensor (Lemaitre and Chaboche, 1994). As discussed previously, in the case of a material plasticized under tension stress, the tensor $\boldsymbol{\sigma}_{int}$ acts as an overall compressive stress state ($\sigma_{int} \leq 0$).

$$\boldsymbol{\sigma}_{int} = \sigma_{int} \begin{pmatrix} 1 & 0 & 0 \\ 0 & -1/2 & 0 \\ 0 & 0 & -1/2 \end{pmatrix} \tag{23}$$

The internal back stress σ_{int} is supposed to increase sharply (in absolute value) during the first hardening stage HS_1 and then to stabilize during the second hardening stage HS_2 (Astie et al., 1981; Feaugas, 1999; Hubert et al., 1999). The following form is chosen:

$$\sigma_{int} = \eta_1\, \sigma_{HS_1} + \eta_2\, \sigma_{HS_2} \tag{24}$$

The proportionality coefficient η_1 can be connected to the relative proportion of hard and soft phases in the polycrystalline material (Cullity, 1972; Hubert and Lazreg, 2017; Maazaz et al., 2021). The regions around the grain boundaries can for instance be considered as harder than the core grains. This coefficient will be used here as an adjustment parameter and identified from the experimental results. The proportionality coefficient η_2 describes the effect of the formation of dislocation structures, stabilizing the internal stresses in the material. Its value is set so as to obtain a constant internal stress at necking:

$$\eta_2 \text{ so that } \frac{\partial \sigma_{int}}{\partial \varepsilon_p}(\varepsilon_p^n) = 0 \tag{25}$$

The internal back stress $\boldsymbol{\sigma}_{int}$ is then simply introduced as an additional term in the magneto-elastic energy (18) by defining the stress $\boldsymbol{\sigma}$ as the sum of the external applied stress $\boldsymbol{\sigma}_{app}$ and the internal stress $\boldsymbol{\sigma}_{int}$:

$$\boldsymbol{\sigma} = \boldsymbol{\sigma}_{app} + \boldsymbol{\sigma}_{int} \tag{26}$$

3.2.2. Introduction of the role of dislocation density

Many works (Seeger et al., 1964; Qureshi and Chaudhary, 1970; Lubitz, 1974; Degauque, 1993) suggested that the initial (reversible) susceptibility χ_i evolves proportionally to $1/\sqrt{N_d}$. Assuming that a similar evolution can be assumed for the initial anhysteretic susceptibility, and considering that the parameter A_s is directly proportional to the initial anhysteretic susceptibility (see Daniel et al. (2008) and Daniel et al. (2015)), it seems natural to incorporate a dependence in N_d for A_s:

$$A_s = \frac{A_s^0}{1 + C\sqrt{N_d}} \tag{27}$$

where A_s^0 is the standard parameter defined by (20) in the virgin (non plasticized) and unstressed material, and C an additional intermediate material parameter.

Keh (1965) and Astie et al. (1981) showed that the average dislocation density of Iron based materials is correlated with the hardening, leading to (28).

$$N_d = \left(\beta\left(K_1 {\varepsilon_p}^{m_1} + K_2 {\varepsilon_p}^{m_2}\right) + \sqrt{N_d^0}\right)^2 \tag{28}$$

where N_d^0 is the initial dislocation density prior to plastic deformation, and β is a proportionality coefficient defined as $1/\beta = 0.76\,G\,b$ in Astie et al. (1981), with b the Burgers vector magnitude for the specimen dislocations, and G the shear modulus of the material.

Considering that the initial dislocation density N_d^0 takes a negligible part in the definition of the dislocation density of the plasticized material, and using (28), the parameter A_s in the multiscale model can be defined as:

$$A_s = \frac{A_s^0}{1 + \eta_d\left(K_1 {\varepsilon_p}^{m_1} + K_2 {\varepsilon_p}^{m_2}\right)} \tag{29}$$

To the price of one additional material parameter η_d, this simple modification of the definition of A_s in the multiscale model allows to describe the decrease of μ_{anh} due to the increase of the dislocation density.

3.3. Identification of modeling parameters

Assuming macroscopic isotropy for the virgin material, twelve parameters are used to describe the behavior of DC04 under plastic strain and reloading stress.

Five parameters (K_1, K_2, m_1, m_2, ε_p^n) are purely mechanical parameters identified from a standard tensile test (see Table 2).

Three other parameters (M_{sat}, A_s^0, λ_{sat}) are obtained from a classical magnetic characterization in the absence of applied stress on the virgin material (no plastic strain). M_{sat} is the maximum magnetization. Its value can be identified from a macroscopic measurement (black curve in Fig. 5(b)) at high field (in practice 3500 A m^{-1} here). A_s^0 (20) can be identified from an anhysteretic measurement (black curve in Fig. 5(b)) at low field (in practice 200 A m^{-1} here). λ_{sat} is the maximum magnetostriction strain Daniel et al. (2014) and Daniel and Hubert (2009). Its value has been measured close to 5.5 ppm from a magnetostriction curve (not shown).

λ'_{sat} is identified by curve fitting from low-field anhysteretic magnetic permeability under uniaxial stress in the elastic regime of the virgin material. In this mechanical state, σ_{int} is set to zero. Here, the curve at $H = 200$ A m^{-1} was used (black curve in Fig. 11). A value of $-4.6\ 10^{-14}$ Pa^{-1} was obtained for λ'_{sat}, corresponding approximately to a reversal stress $\sigma_u^r = 60$ MPa.

η_1 is obtained by fitting one magnetization curve under no applied stress ($\boldsymbol{\sigma}_{app} = \mathbb{0}$) at low plasticity level during HS_1. Here, the curve at $\varepsilon_p = 0.045\%$ was used.

η_2 is set from Eq. (24) by imposing a null derivative at necking (25).

η_d is obtained by fitting one magnetization curve under no applied stress ($\boldsymbol{\sigma}_{app} = \mathbb{0}$) at high plasticity level during HS_2. Here, the curve at $\varepsilon_p = 14.5\%$ was used.

As a summary, all material parameters are identified from a tensile curve, three magnetization curves at null, low (HS_1, 0.045%) and high (HS_2, 14.5%) plasticity levels, and one anhysteretic permeability curve as a function of stress at low magnetic field for the virgin material. The anhysteretic modeling parameters are summarized in Table 3 indicating the values used in this paper.

3.4. Phenomenological parameters related to the dissipation part of the magneto-plastic behavior

The anhysteretic behavior can be seen as the skeleton of the magnetic behavior of the material. Once the anhysteretic behavior has been described, it is then interesting to extend the modeling approach to the full magnetic hysteresis loop. To this end, a phenomenological description of the coercive field and remnant induction as a function of stress and plastic strain is provided in this section.

3.4.1. Coercive field H_c

As discussed in the previous section, H_c is not significantly affected by the application of stress in the case of DC04. On the contrary it is observed that the coercive field is highly dependent on the plasticity level. This is explained by the multiplication of dislocations that act as additional pinning sites. The variation of the coercive field is commonly described through a $\sqrt{N_d}$ dependence (30). By combining this assumption with the expression of the dislocation density (28), and keeping neglecting the value of N_d^0, a simple evolution of H_c as a function of the plastic strain is proposed (31). It introduces the value H_c^0 of the coercive field at zero or very low plasticity level and a proportionality coefficient η_H.

$$\Delta H_c(\varepsilon_p) \propto \sqrt{N_d} \approx \eta_H\left(K_1 {\varepsilon_p}^{m_1} + K_2 {\varepsilon_p}^{m_2}\right) \tag{30}$$

$$H_c(\varepsilon_p) \approx H_c^0\left(1 + \eta_H(K_1 {\varepsilon_p}^{m_1} + K_2 {\varepsilon_p}^{m_2})\right) \tag{31}$$

In practice, H_c^0 (420 A m^{-1}) was obtained from the average values obtained on the unstressed virgin material and on the unstressed material deformed at $\varepsilon_p = 0.045\%$. η_H ($1.40\,10^{-9}$ MPa^{-1}) was obtained from the value of H_c on the major loop of the unstressed material plasticized at high strain level (HS_2, 14.5%). These three curves are the hysteretic counterparts of the anhysteretic curves already used for the identification of the anhysteretic material parameters. The identified parameters are reported in Table 3.

3.4.2. Remnant induction B_r

Assuming, as a first approximation, that the hysteresis major loops can be obtained by shifting the anhysteretic curves by an amount of $\pm H_c$, the remnant induction $B_r(\boldsymbol{\sigma}_{app}, \varepsilon_p)$ is simply obtained from the multiscale model by calculating $B_{anh}(H_c, \boldsymbol{\sigma}_{app}, \varepsilon_p)$, without any additional material parameter.

4. Modeling results for the magneto-elasto-plastic behavior of DC04

The modeling approach proposed in the previous section was run using the material parameters given in Tables 2 and 3. The computational time required to obtain each modeling curve (500 points) is less than one second on a personal computer. The results are discussed hereafter.

Table 3
Anhysteretic (left) and dissipation (right) modeling parameters for DC04.

Parameter	M_{sat}	λ_{sat}	A_s^0	λ'_{sat}	η_1	η_2	η_d	H_c^0	η_H
Value	1.38 10^6	5.5 10^{-6}	7.0 10^{-3}	−4.6 10^{-14}	−0.580	0.354	6.44 10^{-9}	420	1.40 10^{-9}
Unit	A m^{-1}	–	m^3 J^{-1}	Pa^{-1}	–	–	Pa^{-1}	A m^{-1}	Pa^{-1}

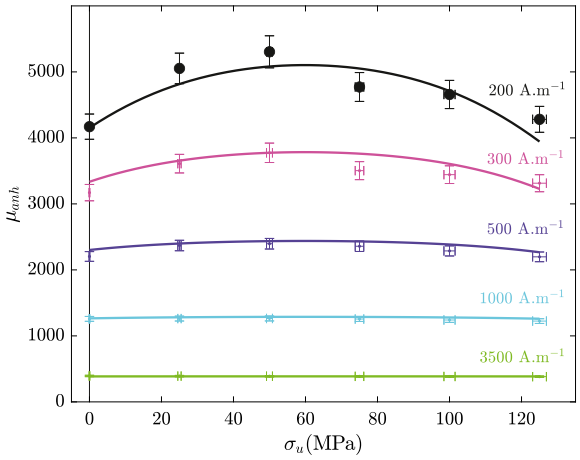

Fig. 11. Experimental (markers with error bars) and modeling (solid lines) results for the anhysteretic magnetic permeability μ_{anh} of DC04 as a function of applied uniaxial stress σ_u at different levels of applied magnetic field H_{anh} for the virgin material ($\varepsilon_p = 0$). The plain markers denotes the experimental data used to determine the modeling parameters M_{sat}, A_s^0 and λ'_{sat}.

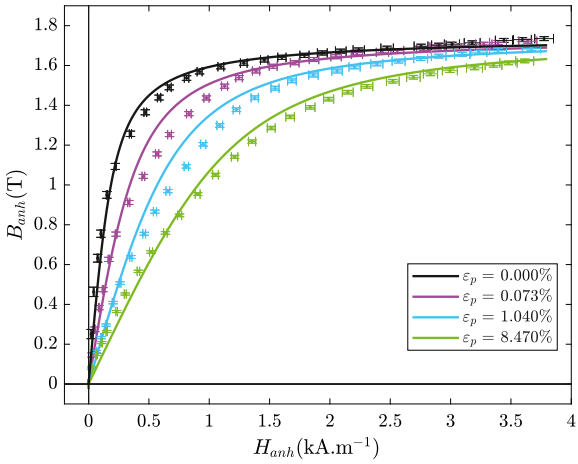

Fig. 12. Experimental (markers with error bars) and modeling (solid lines) results for the anhysteretic magnetic behavior of DC04 under different levels of plastic strain ε_p, in the unloaded state ($\sigma_u = 0$). Two curves ($\varepsilon_p = 0.045$ and 14.5%, not shown here) were used for the identification of the parameters η_1 and η_d.

4.1. Anhysteretic behavior

Fig. 11 shows the comparison between modeling and experimental results for the magneto-elastic behavior of virgin samples of DC04. The data used to identify the modeling parameters M_{sat}, A_s^0 and λ'_{sat} are shown in plain markers. Other curves are blind prediction of the model. Whatever the level of magnetic field, it is evident that the model is able to reproduce the nonlinear evolution of μ_{anh} with stress. This is done with just one additional material parameter (λ'_{sat}) compared to the standard simplified multiscale approach (Daniel et al., 2015). The connection between λ'_{sat} and the reversal stress σ_u^r makes the identification process straightforward.

Fig. 12 presents a comparison between experimental and modeling results for the anhysteretic magnetic behavior of DC04 in the stress-free state for different levels of ε_p. Magnetic behavior obtained in the virgin state (black curve) is correctly reproduced by the modeling tool. An overestimation of the magnetic induction is observed in the saturation knee, which is a known tendency of the multiscale model (Daniel et al., 2008, 2014). The modeling curves obtained both at low and high plastic strain values are close to experimental ones. These results confirm that the introduction of both internal back stress and dislocation density in the multiscale approach allows to correctly reproduce the effect of plasticity on the anhysteretic behavior of DC04 in the first and second hardening stages. The accuracy of the model is slightly more challenged in the transition stage between HS_1 and HS_2, where the effects of σ_{int} and N_d are not clearly distinguished.

Fig. 13 presents the modeling results obtained for various plasticity levels when a reloading stress is applied to the material (see Fig. 3). High field values (above 2 kA m^{-1}) are excluded to focus on the field values for which the sensitivity to stress is stronger. It must be highlighted that the experimental results under reloading stress have not been used at all for the material parameter identification. The quantitative agreement is of course not perfect, which can be explained by the absence of any adjustment procedure for these predictions. However, the main trends of the magneto-elasto-plastic behavior are well described, and notably the non-monotonicity of the effect of tensile stress on the magnetic permeability. This result confirms the relevance of the introduction of a second-order term in the magneto-elastic energy (18).

In order to evaluate the accuracy of the modeling for all values of ε_p and under reloading stress σ_u (0, 50, 100 MPa), Fig. 14 shows the evolution of μ_{anh} at different levels of applied magnetic field H_{anh} (250, 750 and 1250 A m^{-1}). Again, the modeling results are blind prediction, without any use of the corresponding experimental results. Although quantitative discrepancies can be observed, the model is clearly able to predict the major trends of the magneto-elasto-plastic behavior. These results support the introduction of both the effects of internal stress and dislocation density to describe the effect of plastic strain on the magneto-elastic behavior of magnetic materials.

4.2. Dissipation parameters

Formula (31) was implemented to describe the effect of plasticity on the coercive field H_c. Fig. 15 shows the comparison between this formula (plain line) and the experimental measurements (markers). The dashed line in Fig. 15 shows the result that would be obtained by interpolating all available experimental data (leading to $H_c^0 = 380$ A m^{-1} and $\eta_H = 2.14\ 10^{-9}$ Pa^{-1}). The accuracy is of course enhanced, to the price of a loss in predictivity. However, the discrepancies between the modeling and experimental results, even for the full interpolation, suggests that the assumption of proportionality between ΔH_c and $\sqrt{N_d}$ (30), or the expression chosen for N_d (28) may be questioned. Such formula, however, remains an interesting approximation for a first estimate.

Based on the modeling for H_c shown in Fig. 15 (plain line), and following the combination with the anhysteretic multiscale model proposed in Section 3.4.2, the evolution of the remnant induction as a function of plastic strain and stress can be predicted. The results are shown in Fig. 16. Again, it must be noted that the model provides blind predictions, without any use of the targeted experimental results. The general trend is correctly described with a gradual decrease of B_r as the plastic strain increases, and a restoration under tension stress. The dashed lines show the experimental values of B_{anh} taken at the coercive

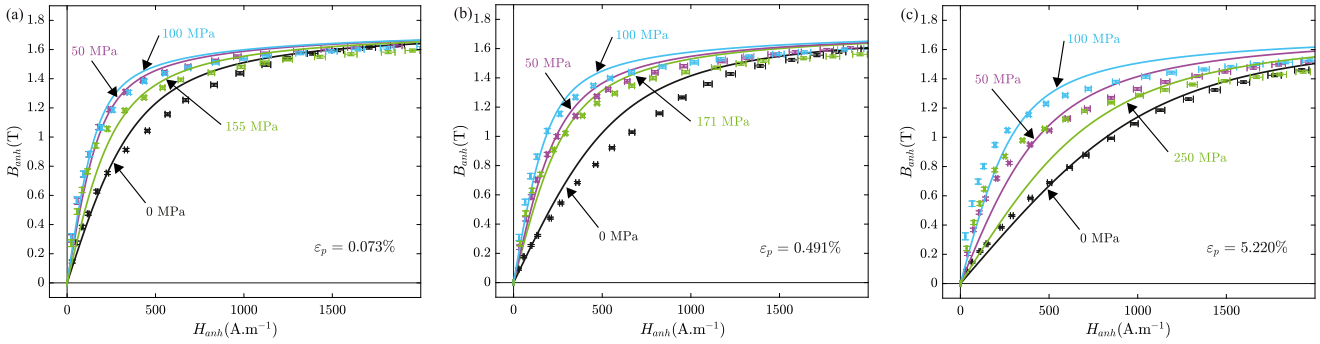

Fig. 13. Experimental (markers with error bars) and modeling (solid lines) results for the anhysteretic magnetic behavior of DC04 under different levels of plastic strain ε_p and reloading stress ($\sigma_u = 0$, 50, 100 MPa and $\sigma_u^{\max}$). None of the experimental results shown in these figures were used for material parameter identification.

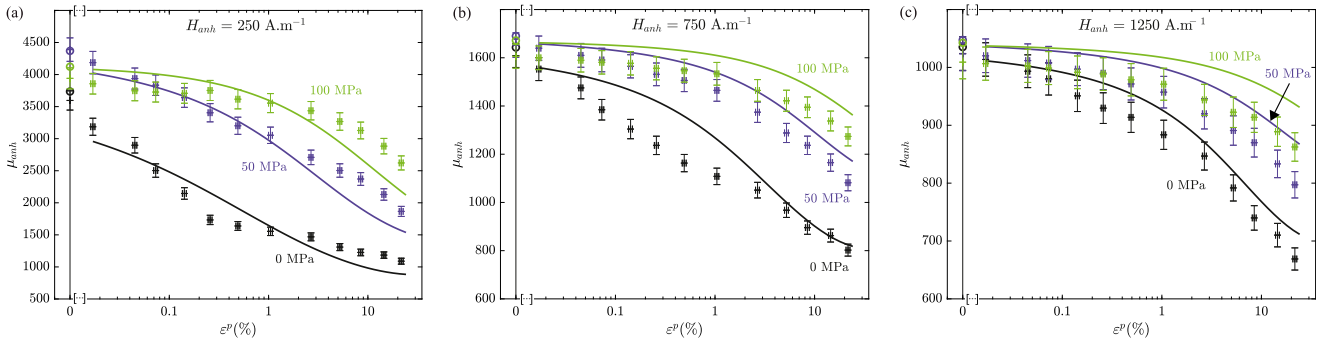

Fig. 14. Experimental (markers with error bars) and modeling (solid lines) results for the anhysteretic magnetic permeability μ_{anh} at H_{anh} = 250 A m^{-1} (a), H_{anh} = 750 A m^{-1} (b) and H_{anh} = 1250 A m^{-1} (c) under different levels of plastic strain ε_p and applied uniaxial stress σ_u.

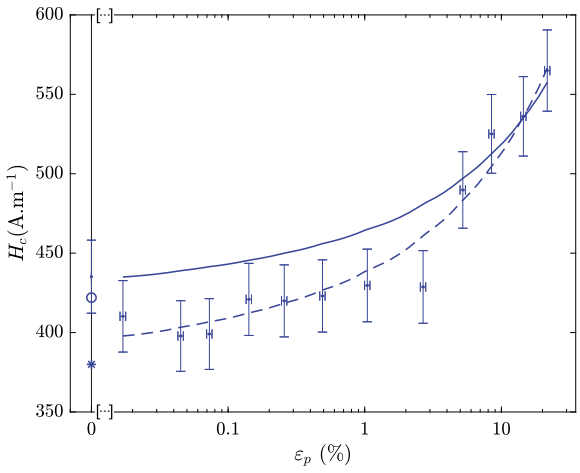

Fig. 15. Experimental (markers with error bars) and modeling (solid line) results for the coercive field of DC04 as a function of the plastic stain ε_p, for $\sigma_u = 0$. The dashed line shows the interpolation obtained using the full set of experimental measurements.

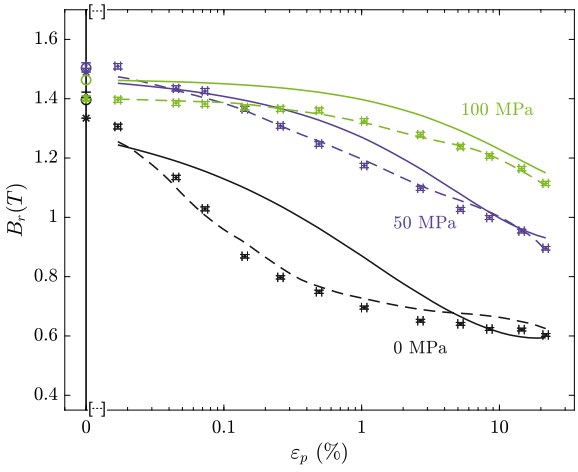

Fig. 16. Experimental (markers with error bars) and modeling (solid lines) results for the remnant induction as a function of the plastic stain ε_p under different levels of applied stress σ_u. The dashed lines show the interpolated values of $B_{anh}(H_c)$ taken from the experimental measurements.

field H_c obtained from measurements. The excellent agreement of this dashed line with the experimental measurements supports the methodology described in Section 3.4.2. The discrepancies between the model (plain lines) and the measurement then necessarily stem from the inaccuracies of the anhysteretic multiscale model (tending to overestimate the magnetic induction) and of the coercive field estimation. However, the proposed modeling provides a relevant estimate for the remnant induction and its evolution under elasto-plastic loading.

5. Conclusion

This work reports the magnetic characterization of an elastically and plastically strained electrical steel (DC04). In addition to classical hysteretic measurements, an anhysteretic characterization was also performed, allowing to clearly distinguish the effects connected to reversible and irreversible phenomena. The mechanical characterization has been conducted in the elastic and plastic regimes. Two hardening stages (HS_1 and HS_2) have been identified with a transition around

1% of plastic strain. These two stages have been associated with two classical plasticity mechanisms and modeled by a modified Ludwik law.

In the relaxed state (no applied stress), the increase of plastic strain ε_p induces a strong degradation of the hysteretic and anhysteretic behaviors from the beginning of the plastic regime. This effect saturates around the transition between HS_1 and HS_2, close to 0.5% of ε_p. Several magnetic characteristics (remnant induction B_r, maximum induction $B_{H_{max}}$, coercive field H_c, and anhysteretic magnetic permeability μ_{anh}) have been extracted from the measurements. They show complex evolutions, correlated to the two hardening stages observed.

For each plasticized state, the magnetic behavior obtained under different reloading stress levels has been measured. It is shown that a reloading stress is able to restore part of the magnetic properties of the virgin material, at least at low field and moderate stress.

Following this comprehensive experimental characterization of the elasto-magneto-plastic behavior, a modeling tool has been developed. It is based on an extension of an existing magneto-elastic multiscale model. The non-monotonicity of the effect of stress on permeability is described by the use of a second order term in the magnetoelastic energy. The effect of plasticity is introduced through two main contributions: the influence of internal stresses due to plasticity and the influence of the evolution of the dislocation density. The identification procedure in order to obtain the modeling parameters is detailed, requiring only a limited number of experimental results. A proposal is also formulated for a phenomenological description of the evolution of the coercive field and remnant induction under elasto-plastic loading.

The comparison between modeled and experimental results of plasticized material in both relaxed and reloaded states showed very satisfying agreement, although the transition between the two stages HS_1 and HS_2 (around 0.5% plasticity) exhibited more discrepancy. This difference can be attributed to the difficulty to clearly distinguish in that region the relative contributions of internal stresses and dislocation density.

The proposed model is a first attempt to provide a robust, compact modeling tool to predict the effect of elasto-plastic loadings on the magnetic behavior. It is important to notice that the model is three-dimensional, allowing to describe the effect of multiaxial magneto-elasto-plastic loadings. This is of primary importance since the processing of materials (cutting, punching, stamping) generates strongly multiaxial deformations, and, once the devices are built, the operational conditions also introduce three-dimensional configurations both in stress and magnetic field. The proposed model is compatible with an implementation into numerical analysis tools and applicable in the full range of plastic strain levels. Many challenges remain to fully validate the approach. The characterization of the magneto-elasto-plastic behavior under multiaxial or non proportional loadings would certainly provide strongly discriminant validation tests. The calculation of magnetic losses is also a necessary extension due to its relevance in magnetic materials applications. Finally, it is also planned to apply the proposed approach to other materials, and particularly other electrical steels under multiaxial testing configurations, in order to provide more evidence of its generality. These aspects constitute the natural perspectives of this work.

Declaration of competing interest

The authors declare that they have no known competing financial interests or personal relationships that could have appeared to influence the work reported in this paper.

Data availability

No data was used for the research described in the article.

Acknowledgments

These results were partially obtained through a partnership with the company Moving Magnet Technologies (MMT), 1 Rue Christiaan Huygens, 25000 Besançon.

Appendix A. Strain gauge measurement

Strain gauges were connected to a strain gauge conditioner and amplifier system using a Wheastone quarter-bridge circuit. The evolution of the strain $\varepsilon_{//}^{eng}$ is given by (32).

$$\frac{u}{U} = \frac{A\, S_g\, \varepsilon_{//}^{eng}}{4}(1-\zeta) \tag{32}$$

where u is the output voltage of the bridge, U the bridge excitation voltage, A the amplification factor, S_g the gauge factor (usually close to 2), and ζ a nonlinearity factor. As detailed in Vishay precision group (2019), in this configuration, this coefficient ζ is expressed as

$$\zeta = \frac{S_g\, \varepsilon_{//}^{eng}}{2 + S_g\, \varepsilon_{//}^{eng}}. \tag{33}$$

Beyond 0.1% of strain, this nonlinearity would induce an error on the strain evaluation higher than 0.1%. As levels of plastic strain are significant, errors due to the Wheastone bridge nonlinearity have been taken into account. The definition of $\varepsilon_{//}^{eng}$ is obtained by combining (32) and (33):

$$\varepsilon_{//}^{eng} = \frac{4\,\frac{u}{U}}{S_g\left(A - 2\,\frac{u}{U}\right)} \tag{34}$$

Neglecting the effect of temperature variation, the accuracy of the gauge measurement is about ±0.5% (Domenjoud et al., 2019).

Three strain gauges (EP-08-125BB) have been glued successively (changed at $\varepsilon_p = 2.67\%$ and $\varepsilon_p = 14.5\%$). The first one was glued using M-Bond 200. The second and the third ones have been glued using M-Bond A-12, specifically adapted to high elongation (beyond 5% strain). S_g is equal to 2.03 for this gauge model. The level of measured noise is shown as ±0.5 ppm (one standard deviation).

Appendix B. Quantification of cross-section measurement error

The error on the evaluation of the cross-section S of the sample depends on the dimensions measurement error and on the influence of neglecting elastic strain. The measurement error using a digital caliper is estimated close to ±0.02 mm.

The quantification of the measurement error has been evaluated using the theoretical values of the cross-section $S^{th}(\varepsilon_{//})$. Based on the assumption of volume conservation during plastic strain Lemaitre and Chaboche (1994), Sth can be expressed as a function of the initial cross-section S_i following (35).

$$S^{th}(\varepsilon_{//}) = \frac{S_i}{1+\varepsilon_{//}^{eng}} \tag{35}$$

The mean value of the relative differences between values of $S^{th}(\varepsilon_{//})$ and measured values $S(\varepsilon_p)$ is about 0.3%.

Appendix C. Anhysteretic measurement procedure

In order to measure the anhysteretic behavior, a sinusoidal current of amplitude I_{max}, reaching $\pm H_{max}$, is first applied on the material to describe a major loop. Then the applied current $I_{anh}(t)$ follows

$$I_{anh}(t) = I_{max}\, \sin(2\pi f t)\, \exp(-kt) + I_b\,(1-\exp(-kt)) \tag{36}$$

where f is the frequency, I_b the bias current value towards which the current exponentially converges, and k a damping parameter described

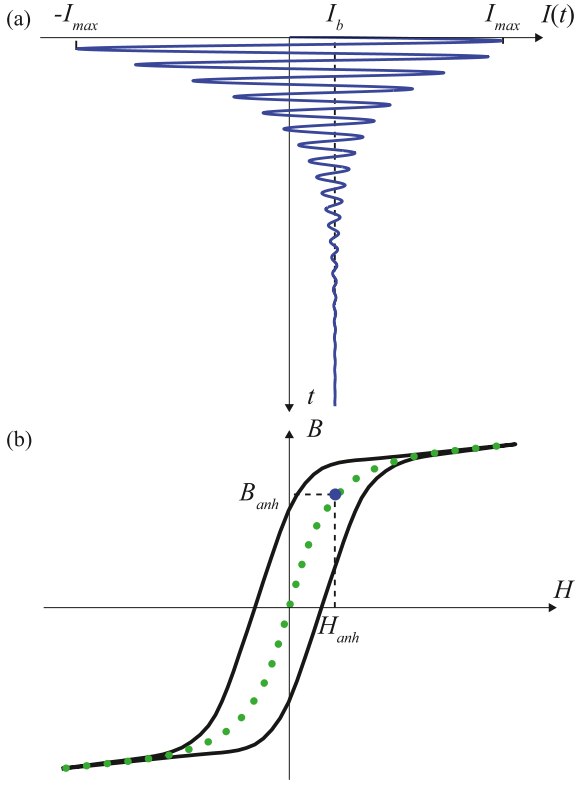

Fig. 17. Representation of the magnetic excitation applied during the anhysteretic measurement process (a) and corresponding anhysteretic point (in blue) of the complete anhysteretic curves (green points) (b). (For interpretation of the references to color in this figure legend, the reader is referred to the web version of this article.)

in Daniel and Domenjoud (2021) (Fig. 17(a)). By varying the value of I_b, the complete anhysteretic curve is obtained (green points of Fig. 17(b)). The anhysteretic behavior is symmetrical with respect to the origin Jiles (1991) and Fiorillo (2004).

At the end of this process, the material induction is noted B_f and could be obtained from (3), assuming that the material was initially demagnetized. This value can suffer from a potential drift in the measurement of B due to the integration process. In order to obtain an accurate measurement of the anhysteretic induction B_{anh}, a last major loop, reaching $\pm H_{max}$ is applied just after the anhysteretic process. During this cycle (see Fig. 18) δB values between 0 and $+H_{max}$ (δB_f) and between $+H_{max}$ and $-H_{max}$ (δB_{max}) are recorded. The maximum magnetic induction (B_{max}) is evaluated (37) and B_{anh} is then calculated following (38).

$$B_{H_{max}} = \frac{1}{2}\delta B_{max} \tag{37}$$

$$B_{anh} = B_{H_{max}} - \delta B_f \tag{38}$$

This procedure ensures an accurate evaluation of the anhysteretic values of the magnetic induction, since the measurement time is much reduced. Moreover, the measurement is made insensitive to a potential residual magnetization after the demagnetization process.

The anhysteretic magnetic induction H_{anh} corresponds to the mean value observed on the last 250 points of the last period of anhysteretic excitation (that represents 0.5% of a period). This way, the noise level on H_{anh} is no more than ± 2.5 A m^{-1}.

As detailed in Domenjoud et al. (2019) and Daniel and Domenjoud (2021), the anhysteretic process is imperfect, resulting for instance in a residual magnetization B_{res} after the demagnetization process. During the experiments presented in this paper, B_{res} always remained under a maximum value B_{res}^{max} of 0.02 T. B_{res}^{max} was observed when the

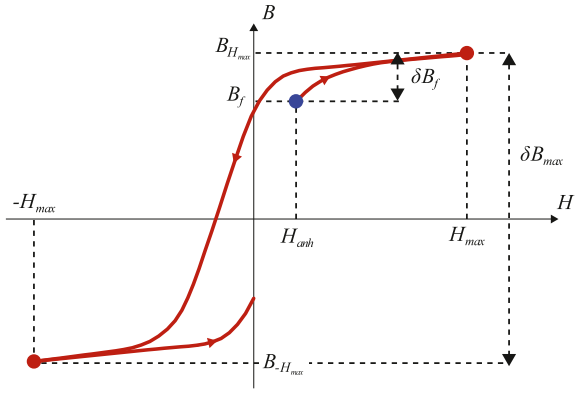

Fig. 18. Major loop obtained after the anhysteretic measurement procedure for an accurate evaluation of the anhysteretic magnetic field B_{anh}. The blue point is the final point of the anhysteretic procedure (Fig. 17) and the red line is the final loading to obtain B_{anh}. (For interpretation of the references to color in this figure legend, the reader is referred to the web version of this article.)

anhysteretic permeability reaches its maximum value μ_{anh}^{max} (≈ 8400 observed in the virgin state, under a stress value of 50 MPa and low field). The existence of this shift in induction results in an error ξ_B in the determination of B_{anh}. This error decreases as μ_{anh} decreases. ξ_B is estimated for each magnetic state using (39).

$$\xi_B(H_{anh}, \sigma_u, \varepsilon_p) = \frac{\mu_{anh}(H_{anh}, \sigma_u, \varepsilon_p)}{\mu_{anh}^{max}} B_{res}^{max} \tag{39}$$

References

Abuku, S., 1977. Magnetic studies of residual stress in iron and steel induced by uniaxial deformation. Japan. J. Appl. Phys. 16 (7), 1161–1170. http://dx.doi.org/10.1143/jjap.16.1161.

Araujo, E.G., Schneider, J., Verbeken, K., Pasquarella, G., Houbaert, Y., 2010. Dimensional effects on magnetic properties of Fe-Si steels due to laser and mechanical cutting. IEEE Trans. Magn. 46 (2), 213–216. http://dx.doi.org/10.1109/TMAG.2009.2034124.

1996. ArcelorMittal 04 (DC04) datasheet. URL http://www.matweb.com/search/datasheettext.aspx?matguid=a3b0be2743384d968c215913322c22c2.

Ashby, M.F., 1970. The deformation of plastically non-homogeneous materials. Phil. Mag. 21 (170), 399–424. http://dx.doi.org/10.1080/14786437008238426.

Astie, B., Degauque, J., Porteseil, J.L., Vergne, R., 1981. Influence of the dislocation structures on the magnetic and magnetomechanical properties of high-purity iron. IEEE Trans. Magn. 17 (6), 2929–2931. http://dx.doi.org/10.1109/tmag.1981.1061496.

Bernard, L., Daniel, L., 2015. Effect of stress on magnetic hysteresis losses in a switched reluctance motor: Application to stator and rotor shrink fitting. IEEE Trans. Magn. 51 (9), 1–13. http://dx.doi.org/10.1109/tmag.2015.2435701.

Bernard, L., Mailhé, B.J., Sadowski, N., Batistela, N.J., Daniel, L., 2019. Multiscale approaches for magneto-elasticity in device simulation. J. Magn. Magn. Mater. 487, 165241. http://dx.doi.org/10.1016/j.jmmm.2019.04.093.

Bertotti, G., 1998. Hysteresis in Magnetism : For Physicists, Materials Scientists, and Engineers. Academic Press, San Diego, http://dx.doi.org/10.1016/B978-012093270-2/50069-6.

Bozorth, R.M., 1951. Ferromagnetism. IEEE Press, New York, U. S..

Bozorth, R.M., Williams, H.J., 1945. Effect of small stresses on magnetic properties. Rev. Modern Phys. 17 (1), 72–80. http://dx.doi.org/10.1103/RevModPhys.17.72.

Buiron, N., Hirsinger, L., Billardon, R., 1999. A multiscale model for magneto-elastic couplings. J. Phys. IV France 09 (PR9), Pr9–187–Pr9–196. http://dx.doi.org/10.1051/jp4:1999919.

Callister, W.D., Rethwisch, D.G., 2014. Materials Science and Engineering: An Introduction. Wiley, Hoboken, NJ.

Craik, D.J., Wood, M.J., 1970. Magnetization changes induced by stress in a constant applied field. J. Phys. D: Appl. Phys. 3 (7), 1009–1016. http://dx.doi.org/10.1088/0022-3727/3/7/303.

Cullity, B.D., 1972. Introduction to Magnetic Materials. Addison-Wesley Pub. Co., Reading, Mass..

da Silva, L.G., Abderahmane, A., Domenjoud, M., Bernard, L., Daniel, L., 2022. An extension of the vector-play model to the case of magneto-elastic loadings. IEEE Access http://dx.doi.org/10.1109/ACCESS.2022.3222833.

Daem, A., Sergeant, P., Dupré, L., Chaudhuri, S., Bliznuk, V., Kestens, L., 2020. Magnetic properties of silicon steel after plastic deformation. Materials 13 (19), 4361. http://dx.doi.org/10.3390/ma13194361.

Daniel, L., Bernard, L., Hubert, O., 2022. Multiscale modeling of magnetic materials. In: Olabi, A.-G. (Ed.), Encyclopedia of Smart Materials, Vol. 5. Elsevier, Oxford, pp. 32–49. http://dx.doi.org/10.1016/b978-0-12-803581-8.12056-9.

Daniel, L., Domenjoud, M., 2021. Anhysteretic magneto-elastic behaviour of terfenol-d: Experiments, multiscale modelling and analytical formulas. Materials 14 (18), http://dx.doi.org/10.3390/ma14185165.

Daniel, L., Galopin, N., 2008. A constitutive law for magnetostrictive materials and its application to Terfenol-D single and polycrystals. Eur. Phys. J. Appl. Phys. 42 (2), 153–159. http://dx.doi.org/10.1051/epjap:2008031.

Daniel, L., Hubert, O., 2009. An analytical model for the ΔE effect in magnetic materials. Eur. Phys. J. Appl. Phys. 45, 31101. http://dx.doi.org/10.1051/epjap/2009012.

Daniel, L., Hubert, O., 2010. Equivalent stress criteria for the effect of stress on magnetic behavior. IEEE Trans. Magn. 46 (8), 3089–3092. http://dx.doi.org/10.1109/tmag.2010.2044561.

Daniel, L., Hubert, O., Billardon, R., 2004. Homogenisation of magneto-elastic behaviour: from the grain to the macro scale. Comput. Appl. Math. 23 (2–3), 285–308. http://dx.doi.org/10.1590/s1807-03022004000200010.

Daniel, L., Hubert, O., Buiron, N., Billardon, R., 2008. Reversible magneto-elastic behavior: A multiscale approach. J. Mech. Phys. Solids 56 (3), 1018–1042. http://dx.doi.org/10.1016/j.jmps.2007.06.003.

Daniel, L., Hubert, O., Rekik, M., 2015. A simplified 3-D constitutive law for magnetomechanical behavior. IEEE Trans. Magn. 51 (3), 1–4. http://dx.doi.org/10.1109/TMAG.2014.2361643.

Daniel, L., Rekik, M., Hubert, O., 2014. A multiscale model for magneto-elastic behaviour including hysteresis effects. Arch. Appl. Mech. 84 (9–11), 1307–1323. http://dx.doi.org/10.1007/s00419-014-0863-9.

Degauque, J., 1993. Soft magnetic materials: Microstructure and properties. Solid State Phenom. 35–36, 335–352. http://dx.doi.org/10.4028/www.scientific.net/SSP.35-36.335.

Domenjoud, M., Berthelot, E., Galopin, N., Corcolle, R., Bernard, Y., Daniel, L., 2019. Characterization of giant magnetostrictive materials under static stress: influence of loading boundary conditions. Smart Mater. Struct. 28 (9), 095012. http://dx.doi.org/10.1088/1361-665x/ab313b.

El Youssef, M., Van Gorp, A., Clenet, S., Benabou, A., Faverolle, P., Mipo, J.-C., 2020. Experimental set up for magnetomechanical measurements with a closed flux path sample. Open Phys. 18 (1), 517–525. http://dx.doi.org/10.1515/phys-2020-0160.

Emura, M., Landgraf, F.J.G., Ross, W., Barreta, J.R., 2003. The influence of cutting technique on the magnetic properties of electrical steels. J. Magn. Magn. Mater. 254–255, 358–360. http://dx.doi.org/10.1016/s0304-8853(02)00856-9.

Feaugas, X., 1999. On the origin of the tensile flow stress in the stainless steel AISI 316 L at 300 K: back stress and effective stress. Acta Mater. 47 (13), 3617–3632. http://dx.doi.org/10.1016/s1359-6454(99)00222-0.

Fiorillo, F., 2004. Characterization and Measurement of Magnetic Materials. Elsevier Academic Press, Amsterdam San Diego, CA, http://dx.doi.org/10.1016/B978-0-12-257251-7.X5000-X.

Gatelier-Rothea, C., Chicois, J., Fougeres, R., Fleischmann, P., 1998. Characterization of pure iron and (130p.p.m.) carbon–iron binary alloy by barkhausen noise measurements: study of the influence of stress and microstructure. Acta Mater. 46 (14), 4873–4882. http://dx.doi.org/10.1016/s1359-6454(98)00205-5.

Gourdin, C., Hirsinger, L., Barbier, G., Billardon, R., 1998. Experimental identification of the coupling between the anhysteretic magnetic and magnetostrictive behaviours. J. Magn. Magn. Mater. 177–181, 201–202. http://dx.doi.org/10.1016/s0304-8853(97)00676-8.

Hubert, O., 2019. Multiscale magneto-elastic modeling of magnetic materials including isotropic second order stress effect. J. Magn. Magn. Mater. 491, 165564. http://dx.doi.org/10.1016/j.jmmm.2019.165564.

Hubert, O., Clavel, M., Hug, E., 1999. Magnetism and internal stresses: Concept of magneto-plastic anisotropy. J. Phys. IV France 09 (PR9), Pr9–207–Pr9–216. http://dx.doi.org/10.1051/jp4:1999921.

Hubert, O., Daniel, L., 2006. Effect of plastic straining on magnetostriction of ferromagnetic polycrystals–experiments and multiscale modeling. J. Magn. Magn. Mater. 304 (2), 489–491. http://dx.doi.org/10.1016/j.jmmm.2006.02.132.

Hubert, O., Daniel, L., 2011. Energetical and multiscale approaches for the definition of an equivalent stress for magneto-elastic couplings. J. Magn. Magn. Mater. 323 (13), 1766–1781. http://dx.doi.org/10.1016/j.jmmm.2011.01.041.

Hubert, O., Daniel, L., Bernard, L., 2022. Multiscale modeling of magnetostrictive materials. In: Olabi, A.-G. (Ed.), Encyclopedia of Smart Materials, Vol. 5. Elsevier, Oxford, pp. 337–354. http://dx.doi.org/10.1016/B978-0-12-803581-8.12058-2.

Hubert, O., Hug, E., 1995. Influence of plastic strain on magnetic behaviour of non-oriented Fe-3Si and application to manufacturing test by punching. Mater. Sci. Technol. 11 (5), 482–487. http://dx.doi.org/10.1179/mst.1995.11.5.482.

Hubert, O., Jendly, N., Daniel, L., 2005. Modelling of the influence of micro-plasticity on the magnetic behaviour of ferromagnetic polycrystals through a multiscale approach. Steel Res. Int. 76 (6), 440–447. http://dx.doi.org/10.1002/srin.200506035.

Hubert, O., Lazreg, S., 2017. Two phase modeling of the influence of plastic strain on the magnetic and magnetostrictive behaviors of ferromagnetic materials. J. Magn. Magn. Mater. 424, 421–442. http://dx.doi.org/10.1016/j.jmmm.2016.10.092.

Hug, E., Hubert, O., Clavel, M., 1996. Influence of the plastic anisotropy on the magnetic properties of a nonoriented 3% silicon iron. J. Appl. Phys. 79 (8), 4571. http://dx.doi.org/10.1063/1.361730.

Hug, E., Hubert, O., Clavel, M., 1997. Some aspects of the magnetomechanical coupling in the strengthening of nonoriented and grain-oriented 3% SiFe alloys. IEEE Trans. Magn. 33 (1), 763–771. http://dx.doi.org/10.1109/20.560110.

Hug, E., Hubert, O., Van Houtte, J.J., 2002. Effect of internal stresses on the magnetic properties of non-oriented Fe–3 wt.% Si and (Fe,Co)–2 wt.% V alloys. Mater. Sci. Eng. A 332 (1–2), 193–202. http://dx.doi.org/10.1016/S0921-5093(01)01722-1.

Iordache, V.E., Hug, E., Buiron, N., 2003a. Magnetic behaviour versus tensile deformation mechanisms in a non-oriented Fe–(3 wt.%)Si steel. Mater. Sci. Eng. A 359 (1–2), 62–74. http://dx.doi.org/10.1016/S0921-5093(03)00358-7.

Iordache, V.E., Ossart, F., Hug, E., 2003b. Magnetic characterisation of elastically and plastically tensile strained non-oriented Fe–3.2%Si steel. J. Magn. Magn. Mater. 254–255, 57–59. http://dx.doi.org/10.1016/S0304-8853(02)00748-5.

Jiles, D.C., 1988. The effect of compressive plastic deformation on the magnetic properties of AISI 4130 steels with various microstructures. J. Phys. D: Appl. Phys. 21 (7), 1196–1204. http://dx.doi.org/10.1088/0022-3727/21/7/023.

Jiles, D.C., 1991. Introduction to Magnetism and Magnetic Materials. Chapman and Hall, London.

Jiles, D.C., Atherton, D.L., Lassen, H.E., Noble, D., deVette, J., Astle, T., 1984. Microcomputer-based system for control of applied uniaxial stress and magnetic field. Rev. Sci. Instrum. 55 (11), 1843–1848. http://dx.doi.org/10.1063/1.1137677.

Keh, A.S., 1965. Work hardening and deformation sub-structure in iron single crystals deformed in tension at 298 °k. Phil. Mag. 12 (115), 9–30. http://dx.doi.org/10.1080/14786436508224942.

Kleber, X., Vincent, A., 2004. On the role of residual internal stresses and dislocations on barkhausen noise in plastically deformed steel. NDT E Int. 37 (6), 439–445. http://dx.doi.org/10.1016/j.ndteint.2003.11.008.

Kuhlmann-Wilsdorf, D., 1985. Theory of workhardening 1934–1984. Metall. Trans. A 16 (12), 2091–2108. http://dx.doi.org/10.1007/bf02670414.

Landgraf, F.J.G., Ragusa, C., Luiz Rodrigues, D., Dias, M.B.S., de la Barrière, O., Mazaleyrat, F., Fiorillo, F., Appino, C., Martino, L., 2020. Loss decomposition in plastically deformed and partially annealed steel sheets. J. Magn. Magn. Mater. 502, 166452. http://dx.doi.org/10.1016/j.jmmm.2020.166452.

Ledoux, Y., Sebastian, P., Samper, S., 2010. Optimization method for stamping tools under reliability constraints using genetic algorithms and finite element simulations. J. Mater Process. Technol. 210 (3), 474–486. http://dx.doi.org/10.1016/j.jmatprotec.2009.10.010.

Lemaitre, J., Chaboche, J.-L., 1994. Mechanics of Solid Materials. Cambridge.

Leuning, N., Steentjes, S., Weiss, H.A., Volk, W., Hameyer, K., 2018. Magnetic material deterioration of non-oriented electrical steels as a result of plastic deformation considering residual stress distribution. IEEE Trans. Magn. 54 (11), 1–5. http://dx.doi.org/10.1109/tmag.2018.2848365.

Li, J., Xu, M., Leng, J., Xu, M., 2012. Modeling plastic deformation effect on magnetization in ferromagnetic materials. J. Appl. Phys. 111 (6), 063909. http://dx.doi.org/10.1063/1.3695460.

Li, T., Zheng, J., Chen, Z., 2016. Description of full-range strain hardening behavior of steels. SpringerPlus 5 (1), http://dx.doi.org/10.1186/s40064-016-2998-3.

Lubitz, K., 1974. Magnetic studies of the dislocation structure of iron single crystals deformed at 295 K. Appl. Phys. 4 (1), 51–61. http://dx.doi.org/10.1007/bf00884153.

Ludwik, P., 1909. Elemente der Technologischen Mechanik. Springer Berlin Heidelberg, http://dx.doi.org/10.1007/978-3-662-40293-1.

Maazaz, Z., Hubert, O., Amira Fnaiech, E., Kassir, L., 2021. Effect of plastic straining on the remanent magnetization of ferritic-pearlitic steel: Experimental and modeling aspects. AIP Adv. 11 (2), 025015. http://dx.doi.org/10.1063/9.0000237.

Makar, J.M., Tanner, B.K., 1998. The in situ measurement of the effect of plastic deformation on the magnetic properties of steel part I - Hysteresis loops and magnetostriction. J. Magn. Magn. Mater. 184 (2), 193–208. http://dx.doi.org/10.1016/S0304-8853(97)01129-3.

Makar, J.M., Tanner, B.K., 2000. The effect of plastic deformation and residual stress on the permeability and magnetostriction of steels. J. Magn. Magn. Mater. 222 (3), 291–304. http://dx.doi.org/10.1016/s0304-8853(00)00558-8.

M'zali, N., Henneron, T., Benabou, A., Martin, F., Belahcen, A., 2021. Finite element analysis of the magneto-mechanical coupling due to punching process in electrical steel sheet. IEEE Trans. Magn. 57 (6), 1–4. http://dx.doi.org/10.1109/tmag.2021.3058310.

M'zali, N., Martin, F., Sundaria, R., Henneron, T., Benabou, A., Belahcen, A., 2020. Finite element modeling of magnetic properties degradation due to plastic deformation. IEEE Trans. Magn. 56 (2), 1–4. http://dx.doi.org/10.1109/TMAG.2019.2951470.

Niechajowicz, A., 2010. Apparent young modulus of sheet metal after plastic strain. Acta Metall. Mater. 55 (2), 409–420.

Ossart, F., Hug, E., Hubert, O., Buvat, C., Billardon, R., 2000. Effect of punching on electrical steels: Experimental and numerical coupled analysis. IEEE Trans. Magn. 36 (5), 3137–3140. http://dx.doi.org/10.1109/20.908712.

Perevertov, O., 2017. Influence of the applied elastic tensile and compressive stress on the hysteresis curves of Fe-3%Si non-oriented steel. J. Magn. Magn. Mater. 428, 223–228. http://dx.doi.org/10.1016/j.jmmm.2016.12.040.

Qureshi, A.H., Chaudhary, L.N., 1970. Influence of plastic deformation on coercive field and initial susceptibility of Fe-3.25% Si alloys. J. Appl. Phys. 41 (3), 1042–1043. http://dx.doi.org/10.1063/1.1658808.

Sablik, M.J., 2001. Modeling the effect of grain size and dislocation density on hysteretic magnetic properties in steels. J. Appl. Phys. 89 (10), 5610–5613. http://dx.doi.org/10.1063/1.1359167.

Sablik, M.J., Jiles, D.C., 1988. A model for hysteresis in magnetostriction. J. Appl. Phys. 64 (10), 5402–5404. http://dx.doi.org/10.1063/1.342383.

Sablik, M.J., Kwun, H., Jiles, D.C., 1987. Model for the effect of tensile and compressive stress on ferromagnetic hysteresis. J. Appl. Phys. 61 (8), 3799–3801. http://dx.doi.org/10.1063/1.338650.

Sablik, M.J., Yonamine, T., Landgraf, F.J.G., 2004. Modeling plastic deformation effects in steel on hysteresis loops with the same maximum flux density. IEEE Trans. Magn. 40 (5), 3219–3226. http://dx.doi.org/10.1109/TMAG.2004.832763.

Schoppa, A., Schneider, J., Wuppermann, C.-D., Bakon, T., 2003. Influence of welding and sticking of laminations on the magnetic properties of non-oriented electrical steels. J. Magn. Magn. Mater. 254–255, 367–369. http://dx.doi.org/10.1016/S0304-8853(02)00877-6.

Seeger, A., Kronmüller, H., Rieger, H., Träuble, H., 1964. Effect of lattice defects on the magnetization curve of ferromagnets. J. Appl. Phys. 35 (3), 740–748. http://dx.doi.org/10.1063/1.1713460.

Shi, P., 2020. Magneto-elastoplastic coupling model of ferromagnetic material with plastic deformation under applied stress and magnetic fields. J. Magn. Magn. Mater. 512, 166980. http://dx.doi.org/10.1016/j.jmmm.2020.166980.

Shi, P., Bai, P., Chen, H.-e., Su, S., Chen, Z., 2020. The magneto-elastoplastic coupling effect on the magnetic flux leakage signal. J. Magn. Magn. Mater. 504, 166669. http://dx.doi.org/10.1016/j.jmmm.2020.166669.

Shi, P., Zhang, P., Jin, K., Chen, Z., Zheng, X., 2018. Thermo-magneto-elastoplastic coupling model of metal magnetic memory testing method for ferromagnetic materials. J. Appl. Phys. 123 (14), 145102. http://dx.doi.org/10.1063/1.5022534.

Stupakov, O., Pal'a, J., Tomáš, I., Bydžovský, J., Novák, V., 2007. Investigation of magnetic response to plastic deformation of low-carbon steel. Mater. Sci. Eng. A 462 (1–2), 351–354. http://dx.doi.org/10.1016/j.msea.2006.02.475.

Thompson, S.M., Tanner, B.K., 1994. The magnetic properties of specially prepared pearlitic steels of varying carbon content as a function of plastic deformation. J. Magn. Magn. Mater. 132 (1–3), 71–88. http://dx.doi.org/10.1016/0304-8853(94)90302-6.

Villari, E., 1865. Ueber die aenderungen des magnetischen moments, welche der zug und das hindurchleiten eines galvanischen stroms in einem stabe von stahl oder eisen hervorbringen. Ann. Phys. Chem. 202 (9), 87–122. http://dx.doi.org/10.1002/andp.18652020906.

Vishay precision group, 2019. Errors due to wheastone bridge nonlinearity. URL http://www.vishaypg.com/docs/11057/tn5071.pdf.

Wang, Z.D., Deng, B., Yao, K., 2011. Physical model of plastic deformation on magnetization in ferromagnetic materials. J. Appl. Phys. 109 (8), 083928. http://dx.doi.org/10.1063/1.3574923.

Zhao, W., Wang, S., Xie, X., Zhou, X., Liu, L., 2021. A simplified multiscale magneto-mechanical model for magnetic materials. J. Magn. Magn. Mater. 526, 167695. http://dx.doi.org/10.1016/j.jmmm.2020.167695.